Progress in Materials Science 142 (2024) 101224

Contents lists available at ScienceDirect

Progress in Materials Science

journal homepage: www.elsevier.com/locate/pmatsci

Kinetic equations and level-set approach for simulating solid-state microstructure evolutions at the mesoscopic scale: State of the art, limitations, and prospects

M. Bernacki

Mines Paris, PSL University, Centre for Material Forming (CEMEF), UMR CNRS, 06904 Sophia Antipolis, France

ARTICLE INFO

Keywords:
Level-set method
Front-capturing approaches
Recrystallization
Grain-growth
Solid-state diffusive phase transformations
Kinetic equations

ABSTRACT

For over three decades, the front-capturing level-set method has demonstrated its prowess for the simulation, at the mesoscopic scale, of numerous mechanisms in the context of microstructure evolution occurring during complex thermomechanical paths. This review delves into the foundations of this numerical framework, charting its evolution concerning polycrystalline materials, examining its recent advancements, scrutinizing its current shortcomings, and exploring future possibilities. Special attention will be given to the context of hot metal forming processes where discontinuous/continuous dynamic recrystallization, post-dynamic recrystallization, grain growth and solid-state phase transformations are the main mechanisms of interest. In this context, this article also aims to reintroduce, as simply as possible, the kinetic equations related to the grain boundary migration.

1. Introduction

The in-use properties of metallic materials are strongly related to their microstructures, which are themselves inherited from the thermomechanical treatments. Hence, understanding, predicting and optimizing microstructure evolution remain open academic questions and are nowadays a key to the competitiveness of major industries, with direct environmental, economic and societal benefits. The prediction of the microstructures take place in the realm of Integrated Computational Materials Engineering (ICME) [1] and the remarkable evolution of computational resources has enabled within the academic world the extensive modeling of solid materials at all scales of interest sometimes with multiscale strategies. In an industrial R&D context, where computational resources are inevitably more limited and codes need to be robust and realistic, macroscale finite element codes with minimal information about the material itself remain the standard.

Indeed, microstructure predictions on multi-pass processes are very challenging due to the strong evolution of the microstructure topology from the beginning to the end of the process. The competition between grain boundary migration due to the minimization of interface energy (grain growth - GG), recovery (RV), solid-state phase transformation (SSPT), dynamic recrystallization (DRX) through nucleation of new grains (discontinuous dynamic recrystallization - DDRX) or rearrangement of substructures (continuous dynamic recrystallization - CDRX), and post-dynamic recrystallization (PDRX), lead to complex coupled effects [2]. Minor variations of the process parameters (interpass and/or reheating times, temperature and strain rate values at each pass) may have huge effects on the way the previous cited mechanisms can take place. In this context, macroscopic and homogenized models, i.e. phenomenological

E-mail address: marc.bernacki@mines-paristech.fr.

https://doi.org/10.1016/j.pmatsci.2023.101224
Received 8 June 2023; Received in revised form 2 November 2023; Accepted 30 November 2023
Available online 9 December 2023

models such as those based on the well-known Johnson–Mehl–Avrami-Kolmogorov (JMAK) equations [3–5] are widely used in the industry, mainly owing to their low computational cost (i.e. with very fast computation times and minimal requirements in terms of memory usage). If this phenomenological framework is quite convenient, the validity range of these models, associated with a given set of material parameters is often limited to a given process and initial material state. To push these limits, mean field models, based on an implicit description of the microstructure by considering grains or precipitates as spherical entities and statistical evolution related to different characteristics (grain size, precipitate size, dislocation density), have been developed [6–13]. Mean-field models generally provide acceptable predictions in terms of recrystallization kinetics, grain size and/or precipitate distribution evolution. However, facing multi-pass processes, they rapidly reach their limits.

Then, there is a tremendous demand for predictive models at the mesoscopic scale which explains the development of the hierarchical scale-bridging strategies, where the so-called mesoscopic "full-field" numerical methods come into play. These approaches, are based on a full description of the polycrystalline microstructure and high-fidelity calculations at the scale of representative volume elements (RVE) where local macroscopic information, such as temperature, strain, and strain rate, determined by macroscopic computations without coupling with the mesoscale characteristics, can serve as boundary conditions. They have demonstrated an exciting potential for an extensive range of microstructure evolutions like the precise modeling of recrystallization [2,14,15] in dynamic or post-dynamic conditions, grain growth [2], diffusive solid-state phase transformations [16], spheroidization [17], and sintering [18].

The primary numerical frameworks involved include Monte Carlo Potts [19–26], cellular automata [27–30,25], multi-phase field [31–33], front-tracking/vertex [34,35], and level-set models [36–39]. These numerical methods are currently used and developed by many researchers [2] and regularly compared for particular metallurgical mechanisms [40,26].

Of course, all the mentioned models have their own strengths and weaknesses. Probabilistic voxel-based approaches such as Monte Carlo Potts and some Cellular Automata formulations are very popular. These models consider uniform grids composed of cells to model microstructure and stochastic laws to predict the motion of interfaces. These simulations are efficient to minimize computational cost and the scalability is excellent. On the other hand, deterministic approaches, based on the resolution of partial differential equations (PDE), are accurate in the description of the involved physical mechanisms although they are numerically more expensive. For instance, front-tracking or vertex approaches are based on an explicit description of interfaces in terms of vertices. Interfaces motion is imposed at each increment by computing the velocity of a set of points. A major difficulty of these approaches is related to the complexity of handling all the possible topological events, such as disappearance and appearance of new grains, which is not straightforward especially in 3D. Other deterministic approaches, also called front-capturing approaches, avoid these topological problems since they are based on an implicit description of the interfaces: the multi-phase field (MPF) and the level-set (LS) methods.

LS simulations in context of regular grids and Fourier transform resolution, with very large number of grains, can be found for grain growth [41,42] and for static recrystallization [43] modeling. When global or local meshing/remeshing operations have to be considered (large deformation, presence of second phase particles…), LS approach in context of unstructured finite element (FE-LS) mesh, and reasonable number of grains can be considered [38,44–48]. One of the major advantages of this approach lies in its ability to simultaneously model numerous concomitant mechanisms in the context of large deformations, which explains its used to simulate realistic industrial thermomechanical paths [49].

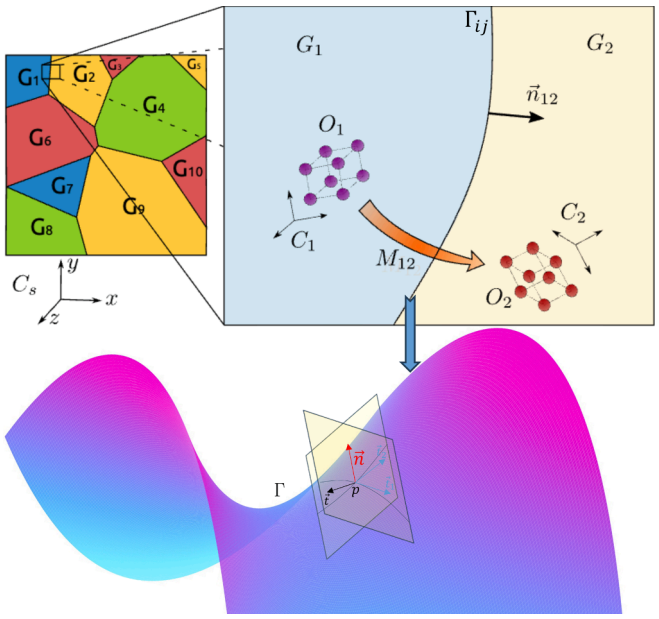

Fig. 1. Scheme depicting one GB and its parameters. Inspired from an image available online at Flickr (https://flic.kr/p/2m5JQkz, Uploaded on 15 June 2021) licensed under CC BY 2.0 (https://creativecommons.org/licenses/by/2.0/). Title: 10GGBParam. Author: Brayan Murgas.

In the following, the state of the art concerning the use of LS method for the modeling of microstructure evolution will be summarized. First, an introduction to the mathematical description of grain boundaries and relevant kinetics equations linked to their evolution will be recalled. Second, the LS methodology in context of polycrystal description will be introduced. Third, algorithms for modeling recrystallization (ReX), GG, and other diffusive phenomena will be described. Discussions concerning the anisotropy of grain boundary energy and how to take into account static or evolving second phase particles (SPP) will be illustrated. Finally some limits, current developments and perspectives of this approach will be discussed.

2. Mathematical description of grain boundaries and kinetic equations of microstructure evolution at the mesoscopic scale

Most common metallic parts have defects that change the structure of the material and their arrangement are responsible of the properties of the material. Defects types can be classified into point (0D), linear (1D), planar (2D) and volume (3D) defects. Vacancies, interstitial, substitutional atoms are point defects, dislocations are 1D defects, grain/phase interfaces, and stacking faults are 2D defects, and pores, cracks are 3D defects. Microstucture evolutions during thermomechanical treatments can be explained by the minimization of the stored energies linked to these different defects. By depicting typical grain boundary network in a polycrystal as in Fig. 1, two neighboring grains $G_i$and G_j constitute a grain boundary (GB) Γ_{ij}. It is characterized by its morphology and its crystallographic properties which may be summarized by a tuple $\mathscr{B}_{ij} = \left(\mathbb{M}_{ij}, \mathbf{n}_{ij}\right)$ with two shape parameters describing the interfaces through the unitary-outward normal direction $\mathbf{n}_{ij}$, and three crystallographic parameters describing the orientation relationship between the two adjacent grains known as the misorientation tensor $\mathbb{M}_{ij}$ (see Fig. 1 top right). This GB space $\mathscr{B}$ parameterized by the misorientation and the normal direction is illustrated in Fig. 1. The misorientation is frequently defined with the axis-angle parameterization, i.e. $\mathbb{M}_{ij}\left(\mathbf{a}_{ij}, \theta_{ij}\right)$, where $\mathbf{a}_{ij}$ is the misorientation axis and θ_{ij} the misorientation angle [50]. The effect of crystallographic symmetries on misorientations is to reduce the fraction of the full orientation space necessary to uniquely represent all possible misorientation relationships. Disorientation tensor describes the misorientation tensor with the smallest possible rotation angle, called the disorientation angle.

As described in Fig. 1, the GB must be mathematically defined as a 2D closed surface with an interior (the grain itself) in a 3D domain Ω, and many driving pressures discussed thereafter are related to metric properties associated with this surface and intrinsic quantities that exist only on it. Therefore, it is necessary to correctly introduce the surface differential operators to describe the characteristics residing on it. Additionally, different ambiguous notation exist in the literature, which can be confusing. Typically, it is common to find in many writings the indices Γ, s, and $\mathbf{n}$ used, sometimes simultaneously. For the sake of consistency with the conventional notation of the GB stiffness tensor [51–53], the '$\mathbf{n}$' index notation referring to the outward unit normal (inclination) will be used in the following to describe all surface-related differential operators on the closed surface Γ. By defining in Ω the sign Euclidean distance $d(\mathbf{x})$ to Γ with positive value inside the closed surface and negative outside (classical in LS framework as discussed in the next section), we have in all points P of $\Gamma, \mathbf{n}_P = -\nabla d(\mathbf{x}_P)$. In the following and for the sake of clarity, the index P will be omitted.. Once $\mathbf{n}$ is clearly introduced, different surface derivative operators and operations for a scalar function $u: \Gamma \rightarrow \mathbb{R}$ and a vector function $\mathbf{u}: \Gamma \rightarrow \mathbb{R}^3$ can be defined:

$$\nabla_{\mathbf{n}} u = \nabla u - (\nabla u \cdot \mathbf{n})\mathbf{n} = \mathbb{P}_{\mathbf{n}} \nabla u = (\nabla u)_{\|}, \tag{1}$$

with $\mathbb{P}_{\mathbf{n}} = \mathbb{Id} - \mathbf{n}\mathbf{n}^T = \mathbb{Id} - \mathbf{n} \otimes \mathbf{n}$ the orthogonal projection,

$$\nabla_{\mathbf{n}} \mathbf{u} = \mathbb{P}_{\mathbf{n}} \nabla \mathbf{u} \ \mathbb{P}_{\mathbf{n}}, \tag{2}$$

$$\nabla_{\mathbf{n}} \cdot \mathbf{u} = \nabla \cdot (\mathbb{P}_{\mathbf{n}} \mathbf{u}) = \nabla \cdot \mathbf{u}_{\|}, \tag{3}$$

$$\Delta_{\mathbf{n}} u = \nabla_{\mathbf{n}}^2 u = \nabla_{\mathbf{n}} \cdot \nabla_{\mathbf{n}} u = \nabla \cdot \nabla_{\mathbf{n}} u, \tag{4}$$

as such a clear framework to introduce the 3D curvature tensor (also called the Weingarten map). It exists different equivalent ways to introduce this tensor. A 2D one, living in the Γ surface, consists to considering the map $P \longrightarrow \boldsymbol{\kappa}$ that assigns each point of Γ to the function that measures the directional curvatures [54] $\boldsymbol{\kappa}(\mathbf{t})$ of Γ at P in the unitary vector $\mathbf{t}$ direction; $\mathbf{t}$ being tangent to Γ at P (see bottom of Fig. 1). The function $\boldsymbol{\kappa}(\cdot)$ is a quadratic form:

$$\boldsymbol{\kappa}(\mathbf{t}) = \begin{pmatrix} \alpha_1 & \alpha_2 \end{pmatrix} \underbrace{\begin{pmatrix} \kappa_{11} & \kappa_{12} \\ \kappa_{21} & \kappa_{22} \end{pmatrix}}_{\mathbb{K}_{|\Gamma}} \begin{pmatrix} \alpha_1 \\ \alpha_2 \end{pmatrix}, \tag{5}$$

where $\mathbf{t} = \alpha_1 \mathbf{t_1} + \alpha_2 \mathbf{t_2}$ with $(\mathbf{t_1}, \mathbf{t_2})$ an orthonormal basis of the tangent space to Γ in $P, \kappa_{11} = \boldsymbol{\kappa}(\mathbf{t_1}),\ \kappa_{22} = \boldsymbol{\kappa}(\mathbf{t_2})$ and $\kappa_{12} = \kappa_{21}$. If the vectors $(\mathbf{t_1}, \mathbf{t_2})$ corresponds to the eigenvectors of the diagonalizable second order tensor $\mathbb{K}_{|\Gamma}$ of corresponding eigenvalues (κ_1, κ_2) as choosen in Fig. 1, then $\kappa_{12} = \kappa_{21} = 0, \kappa_{11} = \kappa_1$ and $\kappa_{22} = \kappa_2$; i.e. the corresponding directional curvatures are known as the principal curvatures. The invariants $det\left(\mathbb{K}_{|\Gamma}\right) = \kappa_1 \kappa_2$ and $Tr\left(\mathbb{K}_{|\Gamma}\right) = \kappa_1 + \kappa_2 = \kappa$ are well-known as the Gaussian curvature and two times the mean curvature. It must be highlighted that, in material science community, the mean curvature is the classical terminology often used to describe the trace itself. A 3D extension of $\boldsymbol{\kappa}$ can easily be obtained by considering the $(\mathbf{n}, \mathbf{t_1}, \mathbf{t_2})$ $\mathbb{R}^3$-orthonormal basis and:

$$\boldsymbol{\kappa}(\mathbf{t}) = \begin{pmatrix} n_1 & \alpha_1 & \alpha_2 \end{pmatrix} \underbrace{\begin{pmatrix} 0 & 0 & 0 \\ 0 & \kappa_1 & 0 \\ 0 & 0 & \kappa_2 \end{pmatrix}}_{\mathbb{K}} \begin{pmatrix} n_1 \\ \alpha_1 \\ \alpha_2 \end{pmatrix}, \tag{6}$$

for any vector $\mathbf{t} = n_1\mathbf{n} + \alpha_1\mathbf{t_1} + \alpha_2\mathbf{t_2}$ and where $\mathbb{K}$ is the curvature tensor, expressed here in the $(\mathbf{n}, \mathbf{t_1}, \mathbf{t_2})$ orthonormal basis. Finally, a classical way to evaluates the curvature tensor in the reference frame consists to use the surface gradient operator defined in Eq. (2). Indeed by using the already precised convention concerning the sign of d and then the sense of $\mathbf{n}$, we have $\mathbb{K} = \nabla_{\mathbf{n}}\mathbf{n} = \mathbb{P}_{\mathbf{n}}\nabla\mathbf{n}\,\mathbb{P}_{\mathbf{n}}$. Interestingly, if the surface gradient operator is quasi-systematically used in the literature to introduced the curvature tensor, it is in fact completely superfluous here. Indeed, by considering firstly that the normal is unitary, and so $\mathbf{n} \cdot \partial_i(\mathbf{n}) = 0\ \forall i$, we have $\nabla\mathbf{n}\,\mathbb{P}_{\mathbf{n}} = \nabla\mathbf{n}$. Moreover, by considering now that Γ is a smooth closed surface, i.e. that $\mathbf{n}$ derived from d and so $\partial_i n_j = \partial_j n_i\ \forall i.j$, we have $\mathbb{P}_{\mathbf{n}}\nabla\mathbf{n} = \nabla\mathbf{n}$. Thus $\mathbb{K}$ and κ can be defined without surface derivative operator as:

$$\mathbb{K} = \nabla\mathbf{n} = -\nabla\nabla d = -Hess(d), \text{ and } \kappa = Tr(\mathbb{K}) = \nabla \cdot \mathbf{n} = -\Delta d. \tag{7}$$

Several metallurgical phenomena have been cited. Therefore, it is important to draw up here an assessment of the kinetics equations existing in the state of the art, at the mesoscopic scale, and their limits and to come back to the relevant physical mechanisms. When ReX and related phenomena or diffusive SSPT are considered, the classical framework consists in defining the interface kinetics as the cross product between a mobility, μ [$m^4 \cdot s^{-1} \cdot J^{-1}$], generally viewed as an intrinsic scalar property of the considered interface and function of temperature, and the considered driving pressures, P [$J \cdot m^{-3}$]:

$$\mathbf{v} = \mu P \mathbf{n}. \tag{8}$$

The first driving pressure of interest, is related to the minimization of the energy correlated to surface defects in materials (as grain and phase interfaces). This energy field [$J \cdot m^{-2}$] is classically denoted γ for GB and σ for phase boundaries (PB). Concerning GB, the corresponding driving pressure can be defined by several way depending on the anisotropy degree of γ. Indeed, as largely exhibited experimentally [2], γ can be seen as a 5-parameter functions $\gamma(\mathbb{M}, \mathbf{n})$. Following the chain rules perfectly depicted by Herring in [55], the capillarity driving pressure P_c linked to a GB interface, moving from the S_0 surface to the $S = S_0 + dS$ surface with a δv resulting volume variation, can be described as:

$$P_c \delta v = -\delta\left(\int \gamma dS\right) = -\int \delta\gamma dS_0 - \int \gamma\delta(dS), \tag{9}$$

with,

$$\int \gamma\delta(dS) \approx \gamma\delta v \mathbb{I}\mathbb{d} : \mathbb{K} = \gamma\delta v Tr(\mathbb{K}), \tag{10}$$

and,

$$\int \delta\gamma dS_0 \approx -\nabla_{\mathbf{n}}\gamma \cdot \mathbf{n}\delta v + \nabla_{\mathbf{n}}\nabla_{\mathbf{n}}\gamma : \mathbb{K}\delta v. \tag{11}$$

By combining Eqs. (9)–(11), we obtain at the first order of the small displacement performed:

$$P_c \approx -\left(\underbrace{\gamma\mathbb{I} + \nabla_{\mathbf{n}}\nabla_{\mathbf{n}}\gamma}_{\boldsymbol{\Gamma}(\mathbf{n})}\right) : \mathbb{K} + \underbrace{\nabla_{\mathbf{n}}\gamma \cdot \mathbf{n}}_{0}. \tag{12}$$

This equation invites various comments. Firstly, as it will be illustrated in Section 3, if the last term is equal, by construction, to 0 for a field existing strictly on a smooth closed Γ interface, this term can become ambiguous if front-capturing type methods are used to describe the interface with an extension of the γ field over a certain thickness around the Γ interface but also near multiple junctions. The term $(\mathbf{n})$ is well known as the GB stiffness tensor [51–53]. Generally, $(\mathbf{n})$ and $\mathbb{K}$ are not diagonalizable in the same basis of orthonormal eigenvectors and the calculation of the tensor double product contracted is not straightforward and must be carefully evaluated in the right basis by also taken into account the dependence of γ to $\mathbb{M}$ and crystallographic symmetries [56,57]. Finally, when γ is assumed not dependent of the inclination $\mathbf{n}$, Eq. (12) simplifies in the well-known mesoscopic kinetic equation for curvature flow:

$$P_c \approx -\gamma(\kappa_1 + \kappa_2) = -\gamma\kappa. \tag{13}$$

Eqs. 12 and 13 are interesting, in my opinion, to discuss the current criticism concerning the real link between GG and curvature thanks to reverse engineering of recent 3D in situ data or 3D full-field high-fidelity simulations [58–60]. Typically, in view of the different proposed equations, the sometimes used recent strong statements that "GB kinetics during GG are not correlated to curvature" is inherently ambiguous. Are we speaking of the trace of the curvature tensor (Eq. (13)) or the curvature tensor itself (Eq. (12))? In the state of the art, it is ultimately the equation (Eq. (13)) that is questioned without taken into account the torque terms in experimental or

numerical analysis. Recent results proposed by Florez et al. [61] seem to reinforce this discussion. The underlying question then being, can one reasonably use equation Eq. (13) in place of Eq. (12) when 3D in situ data at interface scale are considered? Is the Eq. 13 acceptable only when an averaged approach at the polycrystalline scale is considered? These questions, as such as the straightness of the 5-parameter manifold used to describe γ, will likely be widely addressed in the coming years via the development of new algorithms for characterizing the GB stiffness tensor in 3D in situ data.

In the context of ReX and related phenomena [2], P is classically defined as:

$$P = P_e + P_c = \tau[\![\rho]\!] + P_c, \tag{14}$$

where τ [J·m^{-1}] is the dislocation line energy and $[\![\rho]\!]$ [m^{-2}] is the homogenized dislocation density jump across interfaces estimated from the modeling of plastic deformation. At the mesoscopic scale, it is often assumed that dislocation density of each grain under subsequent deformation (ϵ) evolves according the following type equation:

$$\partial_\epsilon \rho = K_1 \rho^{\xi} - K_2 \rho, \tag{15}$$

where K_1 and K_2 are two material constants which respectively describe the strain hardening and the recovery and ξ a model dependent parameter. The well-known Yoshie-Laasraoui-Jonas (YLJ) model [62] corresponds to $\xi = 0$ and Kocks-Mecking one to $\xi = 1/2$ [63,64]. Of course, more precise numerical framework involving crystal plasticity simulations, and many intermediate models in terms of complexity, can also be considered. In context of hot metal forming and large plastic deformation, crystal plasticity finite element method (CPFEM) is often used. In CPFEM, the stress–strain response of each finite element (FE) is defined by a single crystal model following an elastoviscoplastic formulation [65–67] and a Lagrangian framework is often used to update the mesh nodes positions. In this context, the local evolution of the dislocation density is defined through the hardening rule depending of the slip rates $\dot{\gamma}_\alpha$, over all the slip systems α, themselves defined through the adopted flow rule. Typically, for FCC materials, the equivalent crystal plasticity YLJ law than Eq. 15 to described density dislocation evolution is obtained with the following equation:

$$\partial_t \rho = \frac{1}{M}(K_1 - K_2\rho)\sum_{\alpha=1}^{n} |\partial_t \gamma_\alpha|, \tag{16}$$

with M the Taylor factor.

In the context of diffusive SSPT, P is generally defined through the well-known Gibbs–Thomson equation applying onto interphase boundaries:

$$P = [\![G]\!] + P_e + P_c, \tag{17}$$

where $[\![G]\!]$ [J·m^{-3}] is the phase transformation (PT) Gibbs free energy jump at the phase interface between the involved phases. Phase equilibrium and resulting $[\![G]\!]$ evaluation at the interface can be achieved by considering ortho-equilibrium (equilibrium for all components) or para-equilibrium (equilibrium only for the fast diffusional species). Para-equilibrium is often adopted in full-field modeling and generally P_e is not taken into account.

In the context of spheroidization and coalescence of second phase objects or precipitates, the kinetic equations can be summarized as [17]:

$$\mathbf{v} = -\Omega \nabla_{\mathbf{n}} \cdot \mathbf{j}^{\mathbf{s}} \mathbf{n}, \tag{18}$$

with Ω the atomic volume and $\mathbf{j}^{\mathbf{s}}$ the surface atom flux,

$$\mathbf{j}^{\mathbf{s}} = -\frac{\delta_s D_s \gamma_s}{kT} \nabla_n \kappa, \tag{19}$$

and so,

$$\mathbf{v} = \frac{\Omega \delta_s D_s \gamma_s}{kT} \nabla^2_{\mathbf{n}} \kappa \ \mathbf{n} \text{ in case of isotropic } \delta_s D_s \gamma_s \text{ field}, \tag{20}$$

with $\delta_s D_s$ the surface diffusion multiplied by the interface thickness, k the Boltzmann constant and T the absolute temperature. Interestingly, classical misunderstanding in the literature often rises from reading an observable metallurgical phenomenon without considering the underlying physical mechanisms. In other words, the preceding equations quantitatively describe many observable phenomena whose observation may suggest that they have little in common. A few examples to illustrate this point are given here: Ostwald ripening phenomenon is the expression of the long time evolution of the phase equilibrium mechanism defined by Eqs. 8 and 17; surface diffusion mechanism defined by Eq. 18 and Eq. 19 is also of prime importance to explain sintering phenomenon [68] or grooving of GB/PB at free surface; abnormal grain growth (AGG) or critical grain growth (CGG) phenomena can be easily understood as some local heterogeneities of terms defining Eq. 14; Smith-Zener pinning of GB or PB by SPP can be totally explained by the curvature term in Eq. 14, or Eq. 17 respectively, and so on. A recurrent limit of existing numerical frameworks often consists to separately consider each fundamental mechanism despite their concomitant nature and their impact on each other in real materials. Of course, in all the previous discussed mechanisms, the plasticity due to the hot deformation but also potentially induced by the transformation themselves can be finely evaluated/predicted in FE framework and taken into account in the previous migration

equations through the terms $[\![\rho]\!]$.

If Eqs. (8)–(11),12,(13)–(20) represent classical description of a large amount of metallurgical phenomena at the mesoscopic scale during metal forming (i.e. correspond to the prime importance driving pressures), they are nonetheless approximations of lower scale mechanisms. Thus, if these kinetic equations and the description of the corresponding physical mechanisms are indeed in constant evolution and improvement at the grain interface scale [58,59,61], they constitute at the polycrystalline scale and in the metal forming state-of-the-art a thermodynamically/kinematically justified and validated homogenized physical framework. Moreover, it can be easily parameterized through homogenization of dynamic molecular simulation results concerning the description of the interface properties.

3. Level-set function, description of polycrystalline microstructure and meshing adaptation

The LS method was firstly introduced by Dervieux and Thomasset [69] under the terminology of "pseudo-density function" in 1979 before to be extensively formalized and disseminated by the works of Osher and Sethian [70] as a numerical tool to trace the spatial and temporal evolution of interfaces. Interestingly, the *G*-equation introduced in combustion by Forman A. Williams in 1985 [71,72] can also be seen as related to the first developments of the level-set approach. The LS approach was enhanced later for curvature flow problems with multiple junctions [36,37] and applied to recrystallization and grain growth in [38,44,45]. The principle for modeling polycrystals is to deal with a front-capturing description of grains G through LS functions ψ in the space Ω :

$$\begin{cases} \psi(\mathbf{x},t) = \pm d(\mathbf{x},\Gamma(t)), & \mathbf{x} \in \Omega, \quad \Gamma(t) = \partial G \\ \psi(\mathbf{x},t \in \Omega) = 0 & \Leftrightarrow \quad \mathbf{x} \in \Gamma(t), \end{cases} \tag{21}$$

More precisely, and as illustrated in Fig. 2, each sub-domain G (grain) in a given domain Ω (polycrystal) is classically described implicitly by computing the signed distance function $\psi(\mathbf{x},t)$ representing the distance to the sub-domain boundaries $\Gamma(t) = \partial G$ (grain boundaries) with, by convention, a positive value inside of the grain and negative outside. In a P1 (linear) interpolation, the function $\psi(\mathbf{x},t)$ is calculated at each node on the FE mesh as illustrated in Fig. 2 (right side). This choice is also in line with the equations described in the previous section for grain interface properties (see Eq. 7).

Using such an implicit description simplifies the polycrystal description as it has not to be strictly correlated to a discretization of the grain/phase boundary interfaces. The experimental image can be seamlessly integrated into a FE mesh by calculating distance functions to the grayscale values at each grain interface as illustrated in Figs. 3a and 3b. Alternatively, it can be evaluated directly within a regular grid that corresponds to the original experimental data. Moreover, when only statistical data, such as average grain size or grain size distribution, is known, one can construct a digital material model based on representative microstructures [74]. Voronoï or Laguerre-Voronoï tessellations (LVT) are methodologies that can be utilized to generate digital polycrystals made of polyhedral grains, while maintaining adherence to the known data. The Voronoï Tessellation Method (VTM) generates random Voronoï nuclei, and defines each Voronoï cell as the space that is closer to a specific nucleus than to any other nucleus. Despite the accurate geometric correlation between Voronoï tessellations and many cellular structures, VTM has some limitations, one of which is the inability to adhere to a specific statistical volume distribution of cells. Xu and Li [75] identified discrepancies between the statistical properties of grains commonly observed in an equiaxial polycrystal and the results derived from VTM. One approach to enhance traditional VTM is to use the Laguerre-Voronoï Tessellation Method (LVTM), which assigns a radius or weight to each nucleus and reflects this distribution in the Voronoï tessellation [76]. An illustration is depicted in Figs. 3c and 3d. It's worth noting that the main challenge of LVTM is similar to the challenge in creating polycrystal microstructures and powder representative volume elements (RVEs), which is to reflect a given statistical size of spheres with the maximum achievable density. This criterion is not only essential for powder RVEs but also for LVTM in order to minimize disparities between the assigned weight and the resulting final volume of the

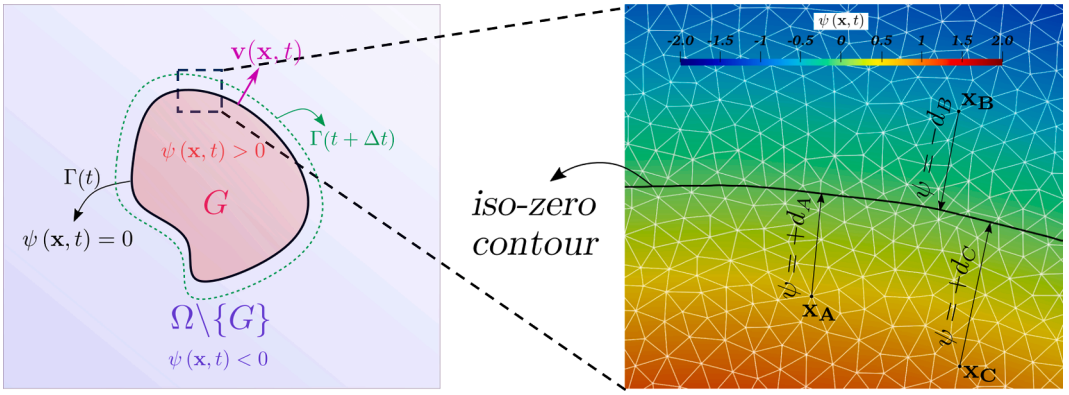

Fig. 2. Inspired from [73]: (left side) Scheme description of a grain defined thanks to a LS function, and (right side) LS field describing a grain in an unstructured FE mesh (in white) in context of a P1 interpolation. The black interface corresponds to a part of the 0-isovalue of the LS, i.e. the grain interface Γ.

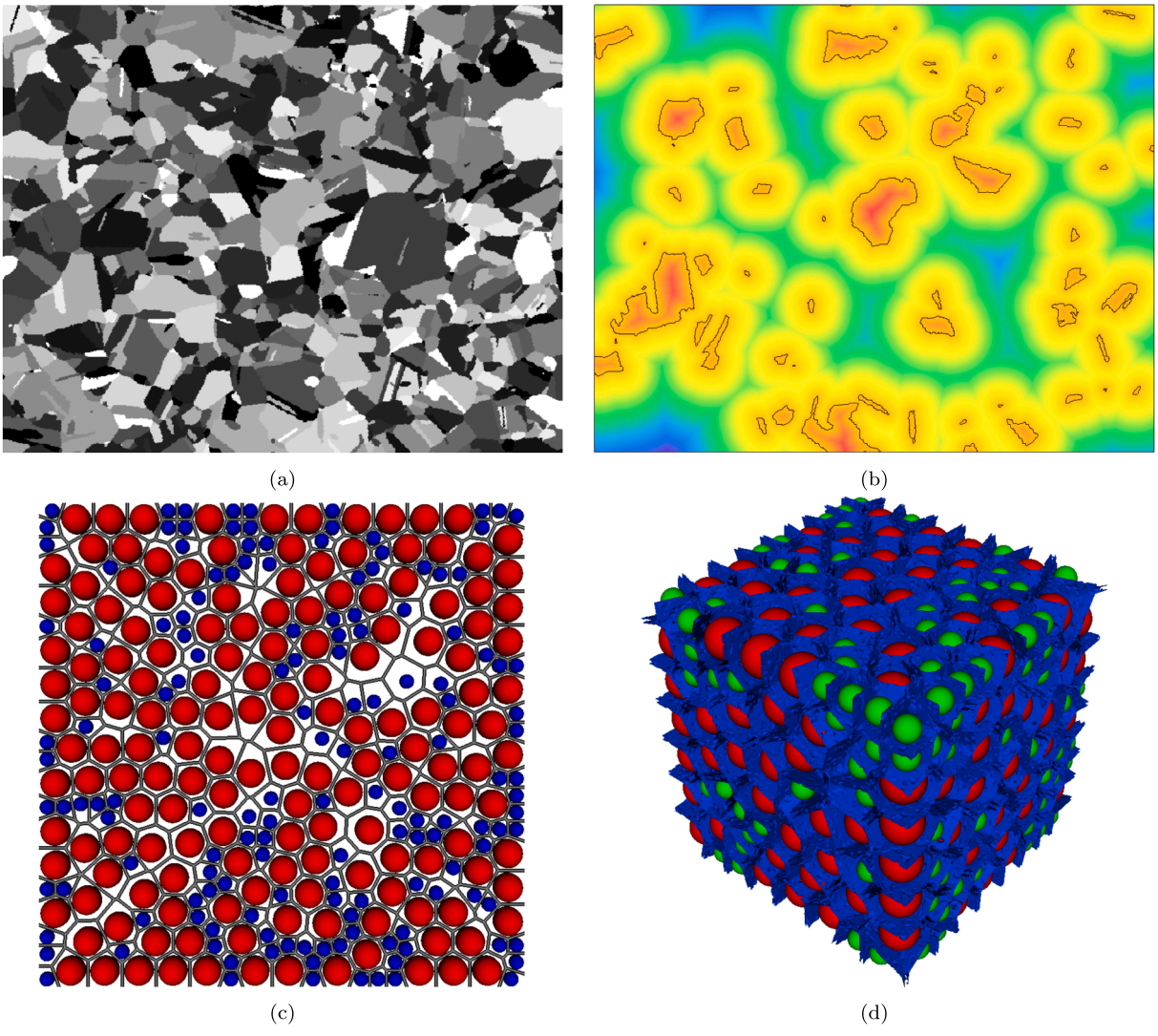

Fig. 3. From [86]: (a) EBSD image obtained from a 304L stainless steel sample, the gray scale refers to the crystallographic orientation, and (b) max of the distance fields of some grains after the FE immersion where the solid black lines indicates the interface of these grains. From [87], illustration of the LVTM method where the radius of each cell is represented: (c) in 2D where the weights are described by the corresponding circles and the resulting GB network is depicted in grey, and (d) in 3D where the weights are described by the corresponding spheres and the resulting GB network is depicted in blue.

Voronoï cells. Although often not clearly discussed in literature, maintaining the radius size distribution for Laguerre-Voronoï sphere packing is distinct from maintaining the grain size distribution for the resulting Laguerre-Voronoï cells. Different strategies have been developed over the past 40 years [77–80], collectively referred to as Sphere Packing Methods (SPM). These methods are typically categorized into two main types: sequential addition models and collective rearrangement models. Both types are employed in the generation of polycrystals [81–85].

In addition to the morphology of the grains or and the phases composition, other attributes playing on the properties of the interfaces or the driving pressures in play can be sought to be respected in an exact or statistical way. The two quantities of interest, the GB energy γ and GB mobility μ, must then be seen, as detailed in Section 2, as functions from the GB space $\mathscr{B}$ to $\mathbb{R}^+$. Thus, when EBSD maps are available, they can be used to define exactly the misorientation map; 3D data allowing to add a complete determination of the $\mathbf{n}_{ij}$ inclination parameter. When these information are missing, a classical strategy consists to use a random grain orientation leading to a Mackenzie-like disorientation distribution function (DDF) [88].

Theoretically, each grain of a single-phase or multi-phase polycrystal should be represented by its own LS function. To decrease computation time and memory usage, non-adjacent grains in the initial microstructure—separated by a certain number of grains δ or a minimum distance—can be grouped to form Global Level Set (GLS) functions using graph coloring techniques. However, this approach makes it impossible to distinguish between grains that share the same GLS function. Consequently, when two child grains of a GLS

grow and meet, numerical coalescence occurs—meaning the grains merge to form one grain. Various strategies can be employed to prevent or minimize numerical coalescence events: for instance, selecting a small initial separation δ or minimum distance to limit computation time while also minimizing coalescence [89], performing complete optimal coloring at each time step, or considering re-coloration algorithms at each time step to manage risky configurations [33,41,90]. Typically, Fig. 3b illustrates one of the GLS function made of non-neighboring grains of the experimental image described in Fig. 3a. It is also important to note that the grain boundary network can always, with or without a coloration strategy, be visualized using the field equal to the maximum of all the considered level-set functions, $\psi_{max}(\mathbf{x},t) = \max_i(\psi_i(\mathbf{x},t))$. This field is positive everywhere and tends toward 0 at the grain boundary network. This continuous function is not differentiable at the GB network and thus cannot be directly used to derive the properties of individual interfaces by calculating its successive derivatives. It should, however, be noted that this field has inspired the most extreme

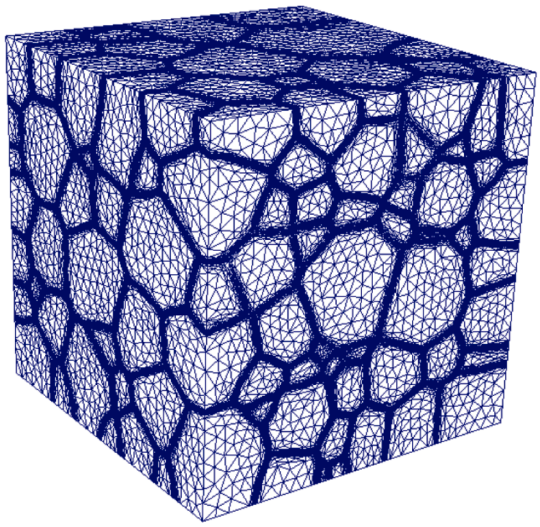

(a)

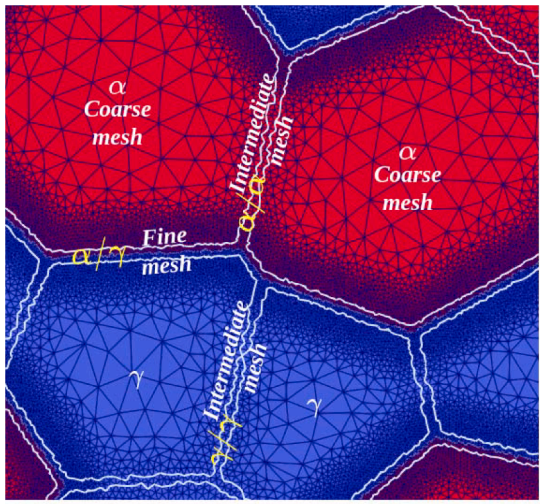

(b)

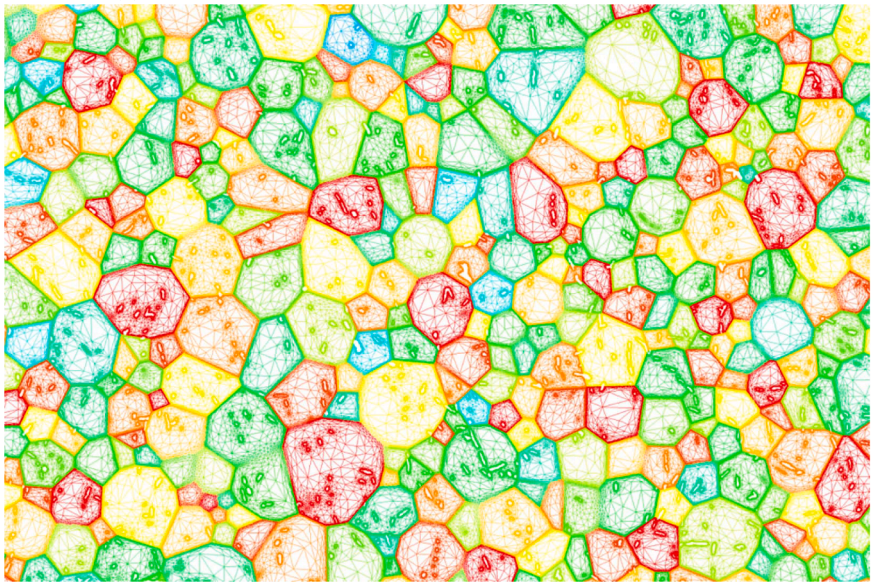

(c)

Fig. 4. (a) 3D equiaxed microstructure example where local anisotropic metric is considered for the FE mesh generation thanks to a posteriori approach [90]. The mesh is adapted to the grain interfaces (generated statistically with a Voronoï tessellation), (b) A 2D two-phase cases where an isotropic strategy is used with a mesh refinement in grain and phase interfaces but with an increased precision in the phase interface [107], and (c) 2D Inconel 718 microstructure example where local anisotropic metric is considered for the FE mesh generation thanks to a geometric approach [99]. The mesh is adapted to the grain interfaces (generated statistically with a Laguerre-Voronoï approach) and to δ phase interfaces immersed thanks to a SEM image. The color code corresponds to the GLS functions.

simplification that can be found to describe polycrystalline microstructure in a LS framework: the Voronoï implicit interface method (VIIM). The basic concept of this approach proposed by Saye and Sethian [91] in 2011 consists of considering only a single level-set function to describe the entire microstructure. This method relies on the interaction between Voronoï diagrams (introduced previously) and an implicit interface method such as the LS method, hence its name. An unsigned distance function maintains a consistent sign (usually positive) within all sub-domains, converging to 0 at the interfaces. Therefore, while it effectively localizes the overall interface network, it does not aim to distinctly differentiate one grain from another during GB migration. More details will be given in the next section.

In the context of polyhedral cells, FE meshing of digital microstructures is typically straightforward. It generally involves discretizing the facets of cells and then the volume within each cell [92]. For real polycrystals observed through Scanning Electron Microscopy (SEM) or 3D X-ray imaging techniques [93,94], approximative Voronoï/Laguerre-Voronoï meshing is not ideal. Though a substantial amount of research has been done on meshing methods for real 3D microstructures [95,96], applying these methods to complex topologies is not an easy task [74,97,98]. The main difficulty lies in dealing with multiple junctions, where balancing respect for experimental data and achieving a high-quality mesh can be complex.

Once a mesh has been generated, modeling large plastic strains and subsequent microstructure evolutions within the FE framework is another significant challenge. Many researchers opt to avoid front-tracking algorithms, where grain boundaries are explicitly meshed, and instead utilize implicit interface methods such as LS and MPF. While results using explicit interface methods are either limited to minor deformations or rely on full reconstruction of the computational mesh at each time step [46], implicit interface methods allow for a wider range of metallurgical phenomena with large deformations [99,90,47,48].

However, this strategy typically demands fine FE meshes at grain interfaces to achieve acceptable accuracy in relation to the driving pressures under consideration. Though global isotropic mesh refinement or high-order interpolation of LS functions can be used to attain desired accuracy in the interface description, these methods substantially increase computational resources. Therefore, adaptive local isotropic or anisotropic remeshing is generally preferred. There are various methods for generating locally adapted meshes to zero-isovalue of LS, but typically, metric field and topological meshers based on local mesh topology optimizations are used [100–102].

Regarding metric calculations, the most common approach is to use a posteriori error analysis to obtain an optimal mesh for a given number of nodes [103–105]. This approach can be extended for situations where a significant number of LS functions must be considered. For instance, when describing strictly disjoint objects with LS functions, one simple solution is to adapt the mesh based on a posteriori error estimator to $\psi_{max}(\mathbf{x},t)$. However, this approach, used in [90,106], is not straightforward when the objects considered are not strictly disjoint, which is the case in polycrystalline microstructures, as the ψ_{max} function is then not differentiable at the grain boundary network.

Alternatively, automatic geometric methods can be employed for creating locally refined isotropic or anisotropic meshes tailored to polycrystals. This is based on the normal and/or mean curvature of the grain interfaces [81,99]. Fig. 4a shows a 3D case for 304L stainless steel where a posteriori metric is adopted [90]. Fig. 4b exhibits a 2D two-phase case where an isotropic strategy is applied. In this case, the mesh refinement occurs in both grain and phase interfaces, but precision is increased at the phase interface [107]. Fig. 4c presents a 2D example where an anisotropic metric is considered using a geometric approach [99] for an Inconel 718 microstructure. The mesh is adapted to the grain interfaces (statistically generated using a Laguerre-Voronoï approach) and to SPP interfaces, which were immersed after thresholding a SEM image.

4. Classical isotropic framework for LS modeling of grain growth and recrystallization

The term 'isotropic' GG or ReX classically refers to the assumption that the properties of the interfaces described during these mechanisms are homogeneous in space. They may vary with temperature and, therefore, over time, but do not vary between the different grain boundaries. This assumption will be progressively relaxed in the Section 5 to discuss the incorporation of the 5-dimensional space discussed in the Section 2. In the LS method, the evolution of $\psi(\mathbf{x},t)$, submitted to a velocity field $\mathbf{v}(\mathbf{x},t)$ as illustrated in Fig. 2 (left side), can be obtained by solving the following convective PDE [69,70]:

$$\begin{cases} \partial_t\psi(\mathbf{x},t) + \mathbf{v}(\mathbf{x},t)\cdot\nabla\psi(\mathbf{x},t) = 0 \\ \psi(\mathbf{x},t=0) = \psi^0(\mathbf{x}) \end{cases} \tag{22}$$

with $\psi^0(\mathbf{x})$ the initial description of the LS function.

4.1. Modeling of isotropic grain growth

In context of deterministic full-field approaches and neglecting torque terms [108], the velocity field can be defined using Eq. 8 and when GG is involved, the net pressure is classically defined using Eq. 13. The isotropy hypothesis remains here, for the LS simulations, to consider γ as constant and μ as only dependent of the temperature through an Arrhenius law $\mu(T) = \mu_0\exp(-Q/RT)$ with μ_0 a pre-exponential constant parameter, R the gas constant and T the absolute temperature. κ and $\mathbf{n}$ can be defined naturally by taking advantages of the possibilities offered by the LS framework. Indeed, considering that GLS functions remain distance functions all along the simulation (i.e. that $\| \nabla\psi(\mathbf{x},t) \| = 1,\ \forall(\mathbf{x},t) \in \Omega\times\mathbb{R}^+$), they can be defined as detailed in Eq. 7 by:

$$\mathbf{n} = -\nabla\psi, \quad \kappa = -\Delta\psi. \tag{23}$$

Finally, by using coloring/recoloring algorithms [90] and the described metric properties of the LS functions, one can solve after substituting Eqs. 23 into Eq. 13 and Eq. 13 into Eq. 8, a set of N_{GLS} convective-diffusive equations as detailed by Eq. 24, with $N_{GLS} \ll N_G$ and $i \in \{1,2,\ldots,N_{GLS}\}$. The numerical strategy consisting in limiting the number of involved LS functions is then generally crucial in terms of numerical cost and memory aspect.

$$\begin{cases} \partial_t \psi_i(\mathbf{x},t) - \mu\gamma\Delta\psi_i(\mathbf{x},t) = 0, \\ \psi_i(\mathbf{x},t=0) = \psi_i^0(\mathbf{x}) \end{cases} \tag{24}$$

The field $\psi_i^0(\mathbf{x})$ is generally defined as the signed distance function to the union of the grains initially present in the ith GLS function, i.e.

$$\psi_i^0(\mathbf{x}) = \max_{j \mid G_j \in GLS_i} \left(d_j(\mathbf{x})\right), \text{ if } \mathbf{x} \in \bigcup_{j \mid G_j \in GLS_i} G_j \text{ and the opposite otherwise.}$$

Generally, a particular numerical treatment must be imposed to avoid kinematic incompatibilities after the resolution of Eq. 24. Indeed, voids can appear at multiple junctions and must be treated. A classical solution consists in correcting the GLS functions as follows [36]:

$$\widetilde{\psi}_i(\mathbf{x},t) = \frac{1}{2}\left(\psi_i(\mathbf{x},t) - \max_{j \neq i}\psi_j(\mathbf{x},t)\right), \quad 1 \leqslant i \leqslant N_{GLS}. \tag{25}$$

The effect of Eq. 25 is schematized in Fig. 5 for a $P1$ interpolation. An alternative could also consist [37] in closing void regions thanks to an energy minimization principle enforced by a Lagrange multiplier related to a constraint added to Eq. 22.

A drawback of the LS formulation lies in the fact that after the resolution of Eqs. (24) and (25), the GLS are no longer distance functions $\| \nabla\widetilde{\psi}(\mathbf{x},t) \| \neq 1$. This is particularly problematic when a specific remeshing technique depending on the distance property is used at the interface as described in the previous section. In addition, the diffusive formulation proposed in Eq. 24 requires a distance function at least in a thin layer around the interface in order to compute properly the curvature driven mechanism. Finally, the conditioning of the transport problem also depends on the regularity of the LS function [99]. For these reasons, the GLS functions need

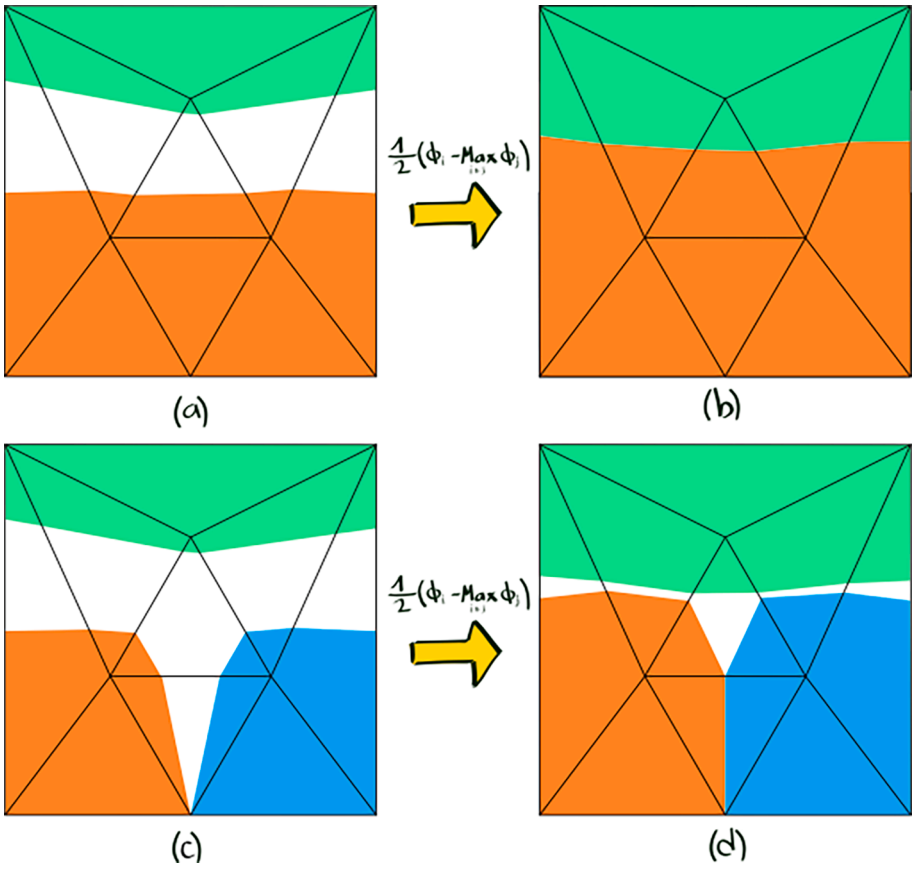

Fig. 5. Global treatment to eliminate non-physical vacuum regions on a FE discretization: two colored LS (a) with a vacuum region in between them, (b) result after applying Eq. (9). Three colored LS: (c) with a vacuum region (d) result after applying Eq. (25). Figure from [109].

to be reinitialized (or redistancing). Restoring the metric property at the instant t is equivalent to solving the following Eikonal equation for each GLS function, i.e. $\forall i \in \{1,2,\ldots,N_{GLS}\}$:

$$\begin{cases} \| \nabla\psi_i(\mathbf{x},t) \| = 1, \ \forall \mathbf{x} \in \Omega \\ \psi_i(\mathbf{x},t) = \widetilde{\psi}_i(\mathbf{x},t) = 0, \ \forall \mathbf{x} \in \widetilde{\Gamma}_i(t) \Leftrightarrow \psi_i(\mathbf{x},t) = \ Redist(\widetilde{\psi}_i(\mathbf{x},t)\,), \end{cases} \tag{26}$$

Different approaches exist to solve this equation including the well-known Fast Marching Method introduced by Sethian [110–112] which propagates a front from the interface and ensures directly a $L2$ gradient norm equals to unity. Though this approach has been extended to unstructured meshes [113], its implementation becomes complicated when it comes to consider anisotropic triangulations [114] and parallel efficiency is poor. Extension velocity approaches proposed by Adalsteinsson and Sethian [115] has also been developed with the idea of maintaining the desired velocity on the interface represented by the 0-isovalue of a distance function, while extending it in a way that naturally respects the conservation of metric properties of the distance function when solving the transport equation. The fast sweeping method was also considered to solve this equation by Zhao and coworkers [116,117]. In [118], a Hamilton–Jacobi (H–J) formulation equivalent to Eq. 26 was proposed in order to correct iteratively the LS values around the interface by solving a PDE. This method is massively used in the FE-LS modeling of ReX and GG [119,89,45,39]. It requires the definition of a purely numerical parameter known as a fictitious time step for reinitialization and the ratio between the desired reinitialized thickness and this parameter gives the number of required increments. Coupled convection-reinitialization (CR) methods emerged wherein the LS function is automatically reinitialized during the resolution of the transport equation [120,38,99]. Their main advantage lies in the fact that only one solver is needed for the simulation instead of two for the classical H–J technique. The signed distance function can also be replaced by any smooth function which satisfies the metric property, at least in a thin layer around the interface. Finally, a natural way to reinitialize GLS functions consists in using a brute force algorithm to perform a complete reconstruction of the distance function. This technique works in two steps: discretize the interface (0-isovalue of the LS function) into a collection of simple elements and, for every integration point, compute the distance to all elements of the collection and store the smallest value which becomes the updated value of the distance function. Though it guarantees optimal accuracy, this Direct Reinitialization (DR) technique is generally reported as being greedy in terms of computational requirements [118,121,122]. It is nevertheless worth mentioning that these works generally address only regular grids or hierarchical meshes [123]. Few years ago, a direct fast and accurate approach usable in unstructured FE mesh has been proposed [124]. This method takes advantage of a space-partitioning technique using $k-d$ tree and an efficient bounding box strategy enabling to maximize the numerical efficiency for parallel computations. Discussions concerning the residual errors inherent to this approach are also proposed in [109].

Interestingly, a similar flow rules than the previously described one can be followed when dealing with the modeling of pure grain growth in regular grids where signed distance functions to interfaces are convolved with Gaussian kernels to generate a variety of geometric motions, including multi-phase motion by mean curvature [41,43,125]. First developments concerning this approach was proposed by Esedoglu, Elsey and coworkers [41,125]. To be more precise, let $d_i^k(x)$ be the signed distance function at times kdt of the ith grain, where dt is the chosen time step. The solution of the curvature flow equation (Eq. 24 with a dimensionless reduced mobility equal to one) for the following time step with d_i^k an initial condition for grain G_i can be obtained as a solution of the heat equation:

$$\tilde{d}_i^{k+1}(\mathbf{x}) = \left(G \star d_i^k\right)(\mathbf{x}), \text{ with } G(\mathbf{x}) = \frac{1}{(4\pi dt)^{dim/2}} e^{-\|\mathbf{x}\|^2/4dt}, \text{ and } dim \text{ the space dimension,} \tag{27}$$

$$\widetilde{\tilde{d}}_i^{k+1}(\mathbf{x}) = \frac{1}{2}\left(\tilde{d}_i^{k+1}(\mathbf{x}) - \max_{j \neq i} \tilde{d}_j^{k+1}(\mathbf{x})\right), \quad 1 \leqslant i \leqslant N_G \tag{28}$$

$$d_i^{k+1}(\mathbf{x}) = Redist\left(\widetilde{\tilde{d}}_i^{k+1}(\mathbf{x})\right), \quad 1 \leqslant i \leqslant N_G. \tag{29}$$

The direct resolution of Eq. 27 obviously allows for unbeatable computation times compared to the FE or finite difference resolution of the isotropic grain growth problem in 2D or 3D. Therefore, much more massive calculations can be proposed [43]. In this case, memory management can become a problem, which explains also the possible use of coloration/recoloration in order to minimize the number of LS function [41]. In this case, Eqs. (27)–(29) are then applied for i ranging from 1 to N_{GLS}. The parallelization of existing formulations has also been considered [126,42,127]. Another expression of G can also be used to improved the approximation of κ or to introduce new terms to the kinetic equation [125]. By the nature of these approaches, based on convolution products on regular grids for solving the heat equation, they have been little extended to the modeling of other mechanisms or enriched in recent years. Any exceptions are cited subsequently.

An alternative of the previous strategies lays in the VIIM method [91,128,129]. this approach is also a PDE-based method but that employs a single function defined on a fixed Eulerian background mesh (regular grids in all the existing literature dedicated to this method). This method tracks evolving interface problems across multiple regions in both two and three dimensions, regardless of the complexity presented by multiply-connected junctions. This method operates by solving the transport equation (Eq. 22) over the chosen time step but for an unsigned distance LS function describing the GB network (and which can be initialized, as discussed in the previous section, as $\psi_{max}(\mathbf{x},t)$). After which, the interface network of interest is reconstructed as the Voronoï interface of the nearby ϵ-isovalue of the LS function. The principles behind the Voronoï interface reconstruction are the same as those of the previously mentioned Voronoï Tessellation Method, but now applied to a set of hypersurfaces (lines in 2D, surfaces in 3D). The reconstructed

Voronoï interface network is then utilized to calculate a new unsigned LS distance function at that moment by solving an Eikonal equation and the velocity field $\mathbf{v}(\mathbf{x},t)$ is updated before initiating a new loop step. Fig. 6 illustrates the Voronoï interface reconstruction around a triple junction (a junction formed by three sub-domains in 2D, analogous to quadruple junctions in 3D).

Two main key points are often highlighted in the state-of-the-art concerning this approach. The first advantage concerns its computational efficiency as only one LS has to considered during all the simulation comparatively to the other LS approaches where few GLS or a large number of LS have to be considered. The second one reported in the literature concerns the fact that the method naturally avoids the management of phenomena such as overlap or decohesion of GB. A slightly different perspective on this second element might be to say that the VIIM approach handles this issue without it being visible thanks to the Voronoï interface reconstruction. To the author knowledge, concerning polycrystalline microstructures of metallic materials, this approach was not yet extended to other mechanisms that isotropic or heterogeneous grain growth or considered for real polycrystals.

4.2. Modeling of isotropic recrystallization

When plastic stored energy as to be considered, the kinetic equation described in Eq. 14 applies and the system defined by Eq. 24 can be rewritten in Eq:30:

$$\begin{cases} \partial_t \psi_i(\mathbf{x},t) - \mu\gamma\Delta\psi_i(\mathbf{x},t) + \mathbf{v}_i^{[\![\rho]\!]} \cdot \nabla\psi_i(v,t) = 0 \\ \mathbf{v}_i^{[\![\rho]\!]} = \mu\tau[\![\rho]\!]_i\mathbf{n}_i, \quad \psi_i(\mathbf{x},t=0) = \psi_i^0(\mathbf{x}) \end{cases} \tag{30}$$

By extrapolating the shape of the velocity term, $\mathbf{v}_i^{[\![\rho]\!]}$ of Eq. 30, for the interface between grain G_i and G_j, the corresponding velocity $\mathbf{v}_{ij}^{[\![\rho]\!]}$ can be written as:

$$\mathbf{v}_{ij}^{[\![\rho]\!]} = \mu\tau[\![\rho]\!]_{ij}\mathbf{n}_{ij}. \tag{31}$$

Classically in LS or MPF approaches, a constant stored energy is considered in each grain [38,99,44,47,46,41,48]. Then, for each interface between grain G_i and G_j, it is assumed that:

$$[\![E]\!]_{ij} = \tau[\![\rho]\!]_{ij} = e_j - e_i, \tag{32}$$

where e_i and e_j are the mean stored energies in the grains G_i and G_j, respectively. These averages can directly come from either constant approximative values where only a gradient of the stored dislocations between the nuclei and the non-recrystallized grains is considered as in [38,45,41], or simplified mechanical formulations as in [48]. They can also be evaluated thanks to an existing dislocation field in the FE mesh of the calculation domain Ω as in [99,44,46,47,130,131] or come from a dislocation density field measured from experimental data, immersed in the FE mesh and averaged per grain as in [132,26,133]. More local approximations of the energetic field can also be considered [134,135].

Special attention has to be paid to the velocity field $\mathbf{v}_i^{[\![\rho]\!]}$ in the vicinity of multiple junctions as emphasized in [38]. In fact, rather than dealing with $\mathbf{v}_i^{[\![\rho]\!]}$ per grain as described in Eq. 30 and considering the contributions of each neighbor as in Eq. 31, a global common velocity can be built in the calculation domain and used for each convection–diffusion system. Generally, the following formulation is adopted:

$$\mathbf{v}^{[\![\rho]\!]}(\mathbf{x},t) = \sum_{i=1}^{N_{GLS}} \sum_{\substack{j=1 \\ j\neq i}}^{N_{GLS}} \chi_{G_i}(\mathbf{x},t)\mu_{ij}\exp\big(-\beta|\psi_j(\mathbf{x},t)|\big)[\![E]\!]_{ij}\big(-\mathbf{n}_j\big), \tag{33}$$

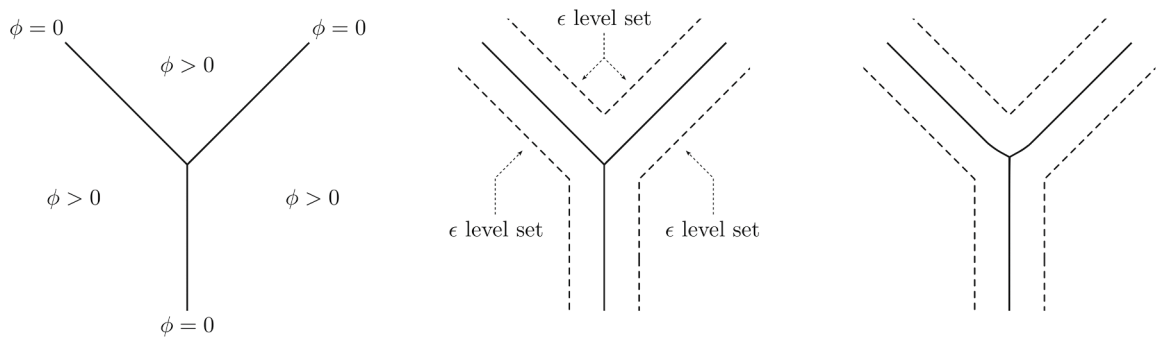

Fig. 6. Reconstruction in 2D of a triple point from an unsigned distance function and the Voronoï interface reconstruction. Figure from [91].

where χ_{G_i} is the characteristic function of the grain G_i, μ_{ij} is the interface mobility between the neighboring grains i and j (equal to μ in isotropic context), the exponential term is a continuous decreasing function varying from 1 to 0 on either side of the interface and has the function of smoothing the velocity field across the interface, β is a positive parameter that controls the degree of smoothness. 3D results obtained this way are summarized in Fig. 7 for a complex thermomechanical path applied onto 304L stainless steel [48]. In this figure, the red circle describes the corresponding position in the thermomechanical path (t(s) in abscissa and T(°C) in ordinate, zigzag lines symbolize deformation steps, straight lines symbolize annealing steps) and the microstructure predicted at the same time with the grain boundary network colored by the stored energy. Fig. 7(a) corresponds to the initial state, Fig. 7(b) corresponds to the beginning of DDRX with appearance of few nuclei at the existing grain interfaces, the deformation is applied along the z-direction with a strain

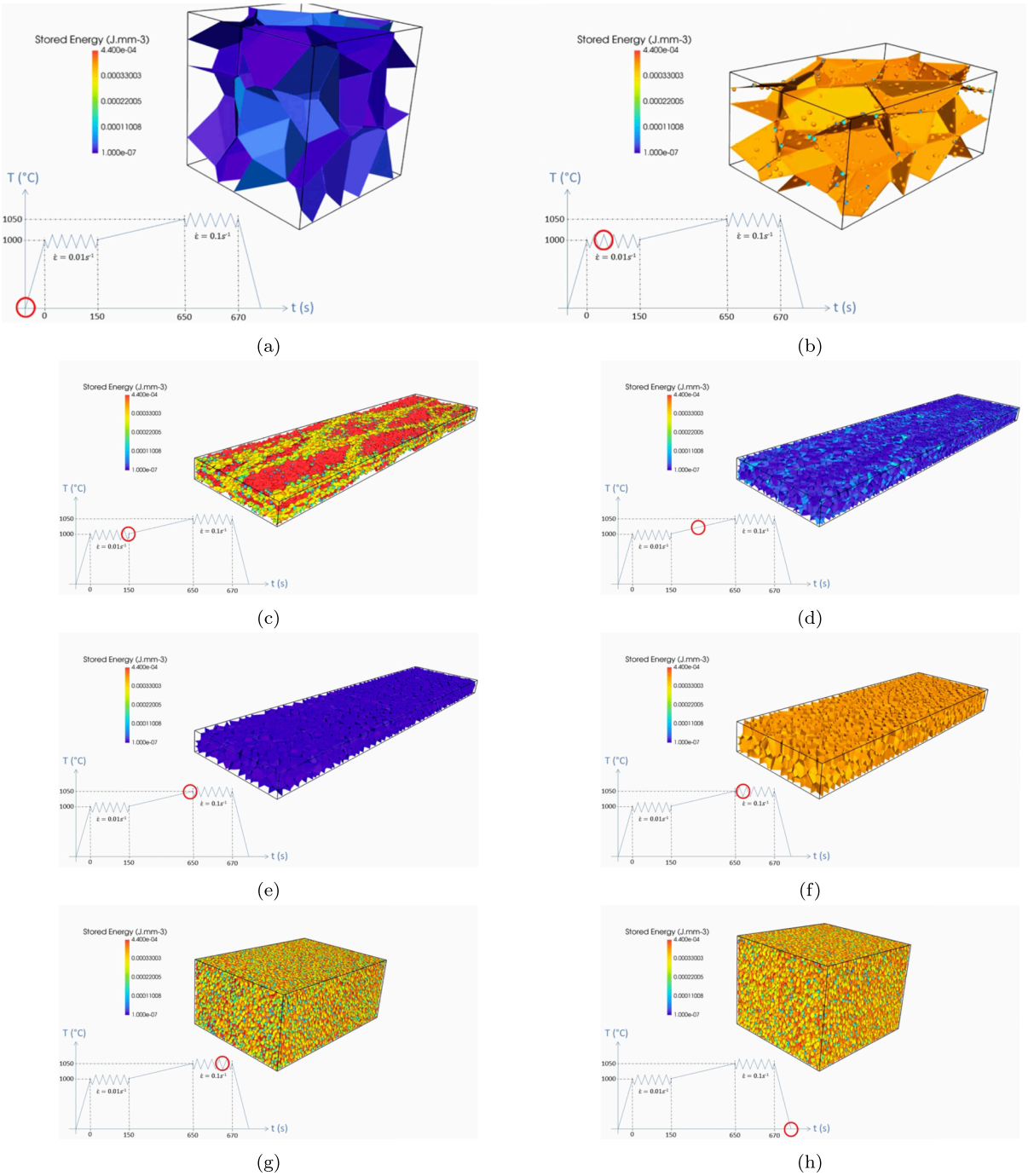

Fig. 7. Complex thermomechanical path for a 304L stainless steel. LS modeling from [48]. A video of this simulation is available online.

rate $\dot{\epsilon} = 0.01s^{-1}$, Fig. 7(c) corresponds to the end of the first deformation; Fig. 7d) and Fig. 7(e) describe the post-deformation evolution during an increase of temperature, MDRX, SRX and GG mechanisms occur; Fig. 7f) and Fig. 7(g) describe a second deformation along the x-direction ($\dot{\epsilon} = 0.1s^{-1}$) with a second DDRX evolution, and finally Fig. 7(h) describes the final state obtained after quenching. The microstructure is initially generated by a Laguerre-Voronoï strategy as detailed in [81]. The system of Eqs. 30 is solved by considering Eqs. 25, 32, 33, an optimized graph recoloration technique [90], a direct reinitialization technique [124] and the simplified mechanical framework detailed in [48] where Eq. 15 is considered (with $\xi = 0$) and associated with a critical stored energy law, a nucleation rate law and a critical nucleus radius law to defined the apparition of recrystallized grains.

Concerning the method based on Gaussian kernels (Eqs. (27)–(29)), it can not be used in context of DRX where domain deformation has to be considered but was extended to take into account a constant stored energy per grain in PDRX evolution context [41].

It must be highlighted that this numerical framework is well adapted for configurations where the anisotropy of GB properties is not of prime importance i.e. where isotropic grain growth and DDRX can be representative of the considered material. This is often the case for low stacking fault energy materials. When texture aspects and subgrain definition, organization and evolution can be of prime importance for microstructure evolution prediction like for high stacking fault energy materials, the discussed framework can become insufficient. In this context, anisotropy of GB interface energy and mobility must be introduced into the LS formalism. This aspect is discussed in the following section.

5. Anisotropy of grain boundary properties and continuous dynamic recrystallization modeling

5.1. LS formulations in context of anisotropic grain boundary properties

The study of GB energy and mobility has garnered significant attention since its initial observation of anisotropy by Smith [136] and Kohara [137]. Existing research has explored two primary modeling approaches: the isotropic approach, where constant values are employed for the GB energy γ and temperature-dependent mobility $\mu(T)$, as introduced in earlier sections [138–140,45,141], and the heterogeneous approach, which proposes energy and mobility values for each grain boundary [142–144,108,145–148,42,149,150]. Heterogeneous models aim to replicate complex microstructures, such as twin boundaries, by accounting for individual grain orientations and the disorientation angle between grains [151,149]. However, the effect of disorientation axis and GB inclination is often overlooked. To address this limitation, anisotropic models have been developed, encompassing the dependence of GB properties on disorientation tensor and inclination [152,153,39,154]. It is essential to clarify the distinction between 3-parameter (heterogeneous) and 5-parameter (anisotropic) full-field formulations, as the literature often ambiguously categorizes heterogeneous GB properties as anisotropic. Additionally, confusion arises between the concepts of respecting an anisotropic GB dynamics and/or respecting Herring's equation at equilibrium [55], with or without considering the torque terms.

The scarcity of GB property data has led to the prevalence of studies utilizing heterogeneous GB properties. Early measurements of GB properties, primarily GB reduced mobility, were conducted on bicrystals [155–160], resulting in the well-known Sigmoidal model [2]. However, advancements in experimental and computational technologies have enabled 3D techniques using X-ray [161–164] or molecular dynamics [165–167] to study GB and recrystallization. At the mesoscopic scale, limited studies have been conducted in 2D using anisotropic GB properties derived from mathematical models [152,153] or by fitting data from molecular dynamics [39]. Nevertheless, these 2D models overlook a portion of the 3D space, as the GB inclination is measured in the sample plane, and GB properties are simplified.

Addressing the study of GB in 3D frequently involves employing heterogeneous GB properties based on mathematical descriptors [168,147,169,170] or databases of GB energy values [171,172]. Two key questions frequently arise in the current state of the art: Can GB properties be accurately described in 2D using classical Read-Shockley [173] and Sigmoidal [2] models? Is the effect of anisotropy stronger in 3D? Answering the latter requires conducting 3D simulations instead of 2D to achieve a more comprehensive description of GB properties in the 5D GB space.

In the current state of the art, four main formulations using a FE-LS approach are notable. The first is the isotropic formulation mentioned earlier, which has been successfully applied to model various annealing phenomena, including GG, ReX, and GG in the presence of SPP [38,99,45,90,48]. While this approach demonstrates good agreement with experimental data in predicting mean grain size and grain size distribution, it may struggle to replicate complex grain morphologies, special grain boundaries, and textures. The second formulation extends the isotropic approach by incorporating heterogeneous GB energy and mobility values through axis-angle parameterization, and even inclination for the energy [174,40].

$$\partial_t \psi - \mu(\mathbb{M}, T)\gamma(\mathbb{M}, \mathbf{n})\Delta\psi = 0. \tag{34}$$

With this formulation, predominant in the LS literature, it is expected to obtain more physical grain shapes. Indeed, some GBs can evolve faster thanks to higher grain boundary mobility values, and triple junctions may have different stable dihedral angles thanks to different GB energy values enabling to respect Herring's equation. This strategy classically used in full-field formulations (not only in LS ones) can lead to confusion when it is named as "heterogeneous". Indeed, *stricto sensu*, the heterogeneity shape of μ *and* γ lead to additional terms in the driving pressure of the kinetic equation (Eq. *14*) as illustrated through Eq. 12 but also in the weak formulation derived to solve the GB motion which are not taken into account in a such strategy. In the following, the term "heterogeneous" will be used to distinguish this formulation from the purely isotropic model. Such strategies were also proposed to deal with heterogeneous description of γ in method based on Gaussian kernels (Eqs. *27,28,29*), one can cite [126,42,175,176]; and also for the VIIM method [128,129] where it was also illustrated in [129] that in the pre-existing heterogeneous VIIM framework, the solution obtained does not

converge to the desired limit (no respect of the equilibrium angles). A such discussion is proposed in [108] where an additional term capturing the local heterogeneity of the multiple junctions is added to the velocity equation such that:

$$\mathbf{v} = \mu(\theta, T)(\nabla\gamma(\theta) \cdot \nabla\psi - \gamma(\theta)\Delta\psi)\nabla\psi. \tag{35}$$

Inserting this term into the transport equation (Eq. 22) leads to the, hereafter called, "Heterogeneous with Gradient" formulation [108]:

$$\partial_t\psi + \mu(\theta, T)\nabla\gamma(\theta) \cdot \nabla\psi - \mu(\theta, T)\gamma(\theta)\Delta\psi = 0. \tag{36}$$

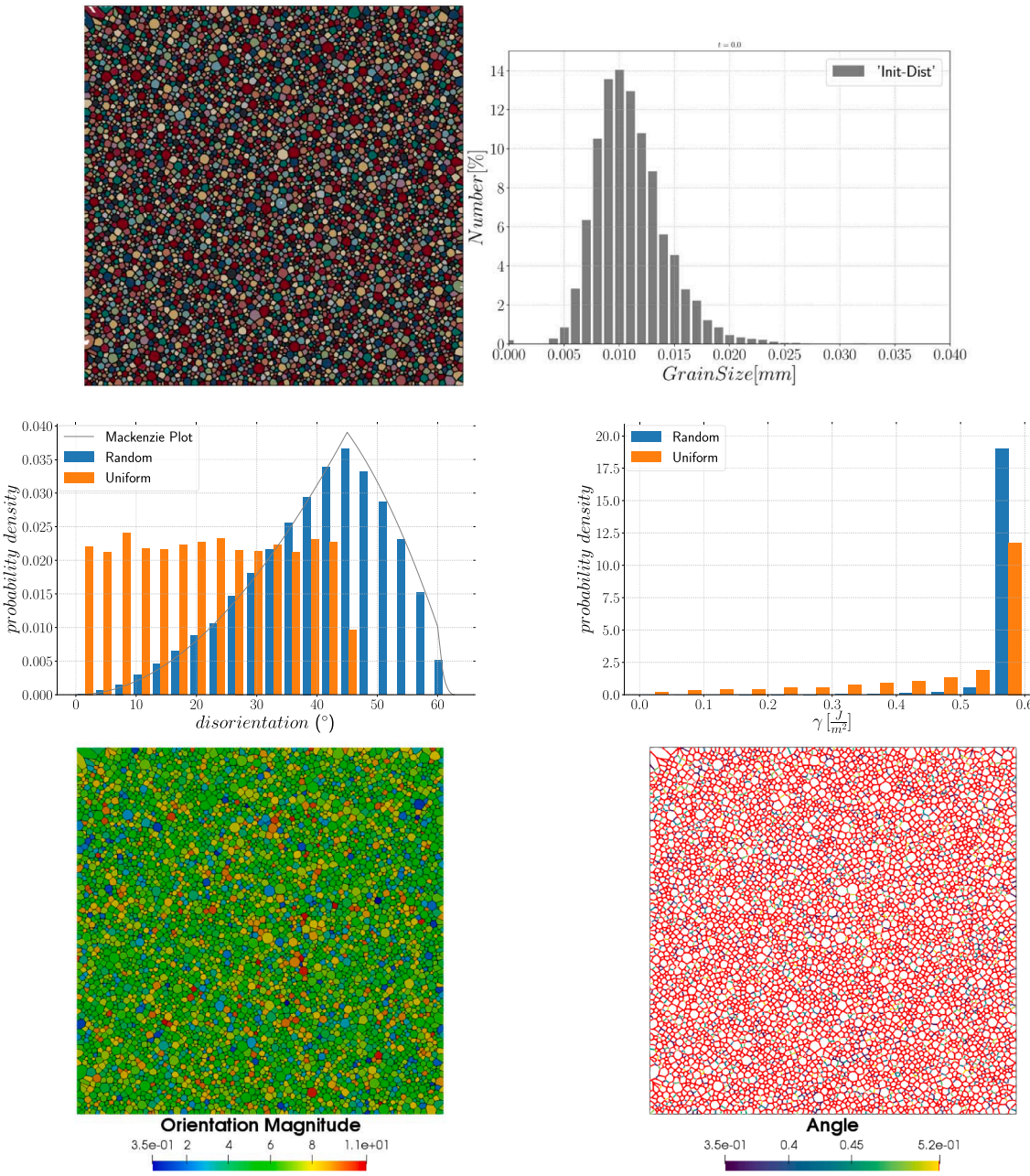

Fig. 8. Characteristics of the initial microstructures (5000 grains) for the anisotropic simulations with from top to bottom and left to right: coloration field of the grain, initial grain radius distribution, initial considered disorientation distributions, initial considered grain boundary energy distributions, orientation magnitude field for the random configuration and disorientation angle field at grain interfaces for the random configuration. From [177].

The introduction of the term $\nabla\gamma(\theta)\cdot\mathbf{n}$ only acts at multiple junctions because these are the only places where this term does not vanish. This formulation is equivalent to the Isotropic one if no heterogeneity is added. The formulation proposed in [39] is very similar. This third formulation was proposed for triple junctions in [108] and extended to model GG using heterogeneous GB energy in [149] and both heterogeneous GB energy and mobility in [177].

The last one is an anisotropic formulation which was initially developed using thermodynamics and differential geometry in [153] and was improved in [177] in order to consider heterogeneous GB mobility. Both the GB normal and misorientation are taken into account and an intrinsic torque term is present:

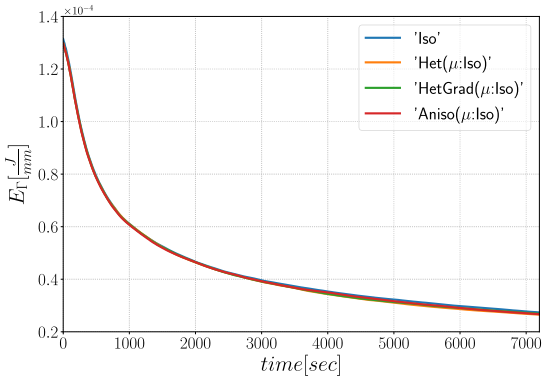

(a) $E_\Gamma = f(t)$ - Random Configuration

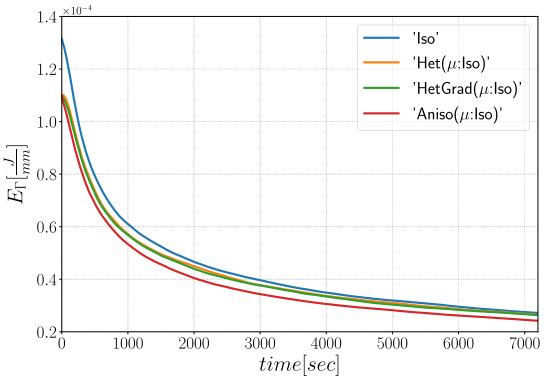

(b) $E_\Gamma = f(t)$ - Uniform Configuration

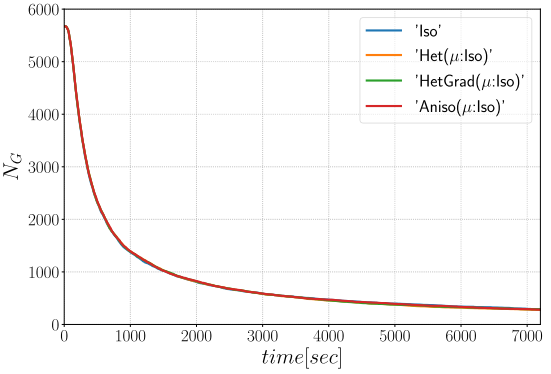

(c) $N_g = f(t)$ - Random Configuration

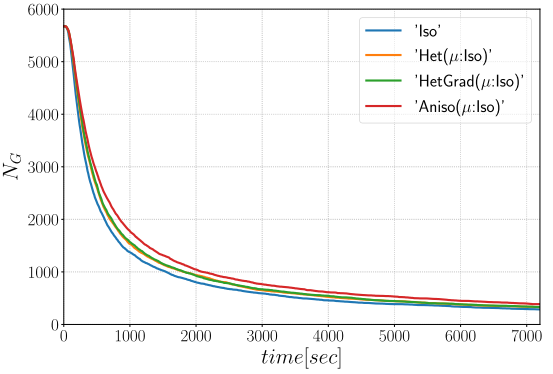

(d) $N_g = f(t)$ - Uniform Configuration

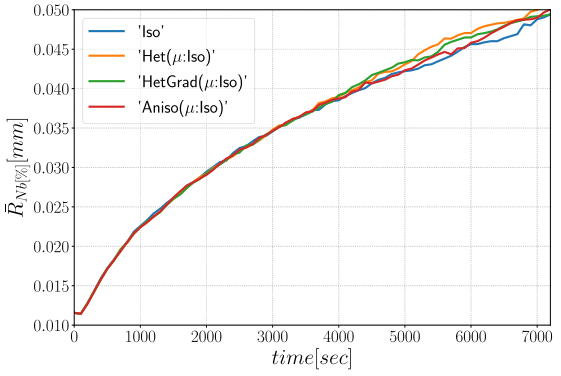

(e) $\bar{R}_{Nb[\%]} = f(t)$ - Random Configuration

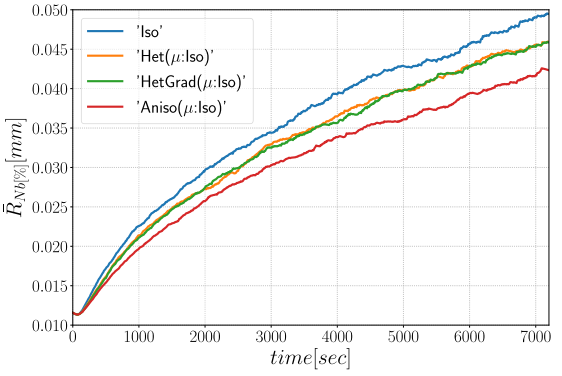

(f) $\bar{R}_{Nb[\%]} = f(t)$ - Uniform Configuration

Fig. 9. Time evolution for the different formulations for the Random configuration in the left side: (a) the total GB energy, (c) the number of grains, and (e) the mean radius weighted in number. Same information for the Uniform configuration are described in the right side. From [177].

$$\mathbf{v} = -\mu\left(\mathbb{M},T\right)\overbrace{\left(-\left(\underbrace{\gamma\mathbb{I}+\nabla_{\mathbf{n}}\nabla_{\mathbf{n}}\gamma}_{\mathbf{\Gamma}(\mathbf{n})}\right):\mathbb{K}+\nabla_{\mathbf{n}}\gamma\left(\mathbb{M},\mathbf{n}\right)\cdot\nabla\psi\right)}^{P_c}\nabla\psi. \tag{37}$$

Remarkably, the term P_c is here totally equivalent to the one introduced in Eq. 12. As detailed in Eq. 12, the term $\nabla_{\mathbf{n}}\gamma(\mathbb{M},\mathbf{n})\cdot\nabla\psi$ in Eq. 37 should be null in the grain interfaces. However, the front-capturing nature of the LS approach which consists to solve Eq. 30 at the GB network and in its vicinity, requires to consider this term which could be non-null around the interfaces near multiple junctions.

In the current state of the art, one can assert that the utilization of these various formulations leads to the observation that predicting grain growth at the polycrystal scale can be ambiguous, contingent upon the targeted attributes and available data. If we bring the discussion of the computational formalism back to its implications for real materials, one can affirm that when untextured polycrystalline materials are involved, the Isotropic formulation can effectively reproduce the evolution of mean grain size and grain size distribution. However, in scenarios with strong texture configurations, the Anisotropic formulation demonstrates superior performance in predicting grain morphology, DDF (disorientation distribution function), and the evolution of interfacial energy, while still maintaining reasonable computational efficiency compared to the isotropic approach. Furthermore, it has been demonstrated that 3D simulations should be considered. This is not only crucial for improving the representativeness of the analyzed polycrystals but also to accurately describe the γ dependence on inclination. The existing 2D models and data currently limit the practical use of inclination.

In addition to this, the integration of torque effects and the GB stiffness tensor in simulations and analysis is an essential aspect that needs to be addressed. It is worth noting that this conclusion is consistent across the majority of existing works in the state of the art involving anisotropic 2D grain growth simulations and 3D simulations, where the inclination dependence, torque terms, or both are not accounted for. To the author's knowledge, only one paper dedicated to the extension of the classical isotropic kernel using Gaussian kernels has been focused on incorporating the γ dependence on inclination, and it was validated in configurations without multiple junctions [178]. This need also implies the necessity of more database dedicated to the extrapolation of the energy of an arbitrary boundary in the different crystallographic systems in link with the five macroscopic degrees of freedom for GB and which can be obtained through embedded-atom method interatomic potentials [179,180]. This discussion is also crucial in the accurate consideration of the behavior of coherent twins, their evolution, their real impacts on the kinetics of non-special grain boundaries, as well as their criteria for appearance during heat treatments. This remains an open subject in terms of physical understanding, polycrystal-scale simulation, and the generation of representative 3D data [181].

To illustrate this discussion, Fig. 8 illustrates the characteristics of a 2D initial example discussed by Murgas et al. [177]: it consists of a square domain with length $L = 1.6mm$ and 5000 grains generated using a Laguerre-Voronoï tessellation [81].

A misorientation dependent GB energy defined with a Read-Shockley (RS) function [173] is considered:

$$\gamma(\theta) = \begin{cases} \gamma_{max}\dfrac{\theta}{\theta_{max}}\left(1-ln\left(\dfrac{\theta}{\theta_{max}}\right)\right), & \theta < \theta_{max} \\ \gamma_{max}, & \theta \geqslant \theta_{max} \end{cases} \tag{38}$$

where γ_{max} is the maximal GB energy. $\theta_{max} = 15°$ is the disorientation angle defining the transition from a low angle grain boundary (LAGB) to a high angle grain boundary (HAGB). $\mu = 1.379\text{J}\cdot\text{mm}^{-2}$, and $\gamma_{max} = 6\times10^{-7}\text{J}\cdot\text{mm}^{-2}$, which are typical for a stainless steel [89], are considered. Two ways are used to exacerbate the GB heterogeneities. In a first one (called Random), the Euler angles defining the crystallographic orientations are generated randomly, leading to a Mackenzie-like disorientation distribution function [182]. In a second one (called Uniform), one Euler angle is generated randomly with a uniform distribution function and the two others are constants. As a result, the final disorientation distribution is more uniform. Both considered orientation distribution and resulting grain boundary energy distribution (GBED) are described in *Fig. 8* (middle) and the resulting orientation field using the vector magnitude $O_G = \sqrt{\varphi_1^2+\phi^2+\varphi_2^2}$ where $(\varphi_1,\phi,\varphi_2)$ are the three Euler angles is described in *Fig. 8* (bottom) for the Random configuration.

The time evolution are summarized in *Fig. 9*. First, it is noticeable that all the formulations have a similar evolution concerning the total grain boundary energy E_Γ, the number of grains N_G and the mean grain size weighted in number $\overline{R}_{Nb[\%]}$ when the Random configuration is considered whereas more stronger GB heterogeneities has a significant impact on the different attributes of the microstructure when the different formulations are adopted. This aspect corroborates the fact to avoid an isotropic formulation when a textured configuration exists in the material.

Another interesting aspect to deal with GB heterogeneities is be able to consider materials where the substructure (LAGBs) are of prime importance in ReX mechanisms as illustrated in the following subsection.

5.2. Continuous dynamic recrystallization modeling

As already highlighted, the LS-FE approach was largely considered in context of DDRX for low stacking fault energy materials by associated Eq. 15 to a critical stored energy law, a nucleation rate law and a critical nucleus radius law. For high stacking fault energy materials, the progressive formation and evolution of subgrains must be taken into account. Dislocations could rearrange themselves to form new LAGB or accumulate into preexisting LAGB. This last phenomenon is responsible for a progressive increase of LAGB misorientation [2,183]. During recrystallization, recrystallized grains form slowly and continuously during deformation. Indeed, in

this CDRX context, grain formation is induced by the progressive reorganization of dislocations into cells or subgrains and the gradual increase of misorientation angle between those subgrain. Recently, a first LS-FE framework was proposed by Grand et al. [184,133,185,135] in order to deal with this mechanism. In these works, laws introduced by the Gourdet-Montheillet model were implemented [186], and while keeping the global dislocation density evolution law defined by Eq. 15, several mechanisms of evolution of dislocations are taken into account:

- rearrangement into LAGB that bound new subgrains. Subgrain formation is described through following equation [186]:

$$dS^{+} = \frac{\alpha b K_2 \rho d\varepsilon}{\eta \theta_0}, \tag{39}$$

  where dS^{+} is the surface of LAGB created. $\alpha = 1 - \exp\left(\frac{D}{D_0}\right)^{m}$ is a coefficient describing the fraction of dislocations recovered to form new subgrains. D is the grain diameter, D_0 is a grain reference diameter and m is a fixed coefficient. η is the number of sets of dislocations and θ_0 the disorientation of newly formed subgrains.
- Stacking into preexisting LAGB which is modeled according to the following equation [186]:

$$d\theta = \frac{b}{2\eta}(1-\alpha) D K_2 \rho d\varepsilon. \tag{40}$$

- Absorption during HAGB migration. This is naturally captured by affecting to the areas swept by moving boundaries a low dislocation density as described earlier.

At each time step, dislocation density of each grain is updated using equation Eq. 15 which impacts the computation of the velocity term related to stored energy differences. Then, the length of subgrain interfaces formed into each grain is computed using Eq. 39. Subgrains can be added grain by grain based on the value of this grain property or globally, after having summed the length of subgrain interfaces for all grains. Subgrain orientation is initialized by applying a small disorientation to the parent grain orientation. The disorientation angle is selected to respect a distribution measured experimentally whereas the disorientation axis satisfies a uniform distribution. The disorientation axis attributed to a subgrain at its formation is kept constant. Then, during time increments, the disorientation angle increase described by Eq. 40 is realized by rotating of $d\theta$ around this axis.

An illustration of this framework in context of CDRX modeling for Zircaloy-4 (Zy-4) was proposed by Grand et al. and is depicted in Fig. 10 after the deformation (the time scale corresponds to the time after the end of the deformation). The initial microstructure

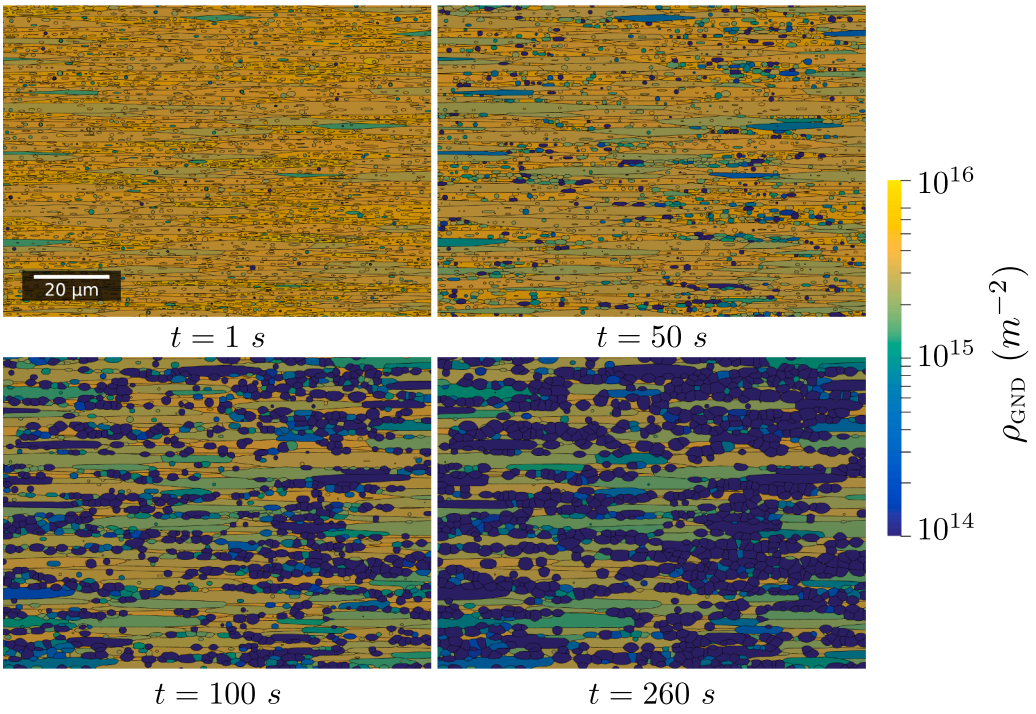

Fig. 10. Illustration of CDRX modeling for Zy-4 thanks to a LS-FE approach from [184]. The time scale corresponds to the time after the end of the deformation. A complete video is available online.

includes approximately 300 grains. The initial number of grains is taken low since it will increase substantially during deformation. Material parameters have been estimated based on the experimental results obtained conducting a thermomechanical testing campaign associated with extensive EBSD characterization. Thermomechanical conditions corresponding to these simulations are the following: $T = 650°C$; $\dot{\varepsilon} = 1.0s^{-1}$; $\varepsilon = 1.35$. The number of subgrains that are formed at each deformation increment is computed individually per grain/subgrain. GB energy is described by the RS equation Eq. 38 and GB mobility is assumed isotropic.

6. Static/evolutive second phase particles

Smith-Zener pinning phenomenon, where precipitates act as obstacles to the displacement of the grain boundaries and may hinder recrystallization and grain growth, was first discussed by Smith [136] and then detailed by Zener one year after [187]. Under certain conditions, SPP can strongly pin the microstructure, leading eventually to a limiting mean grain size (MGS). Since these first developments to equate this phenomenon, many variants have been developed in order to dispel some of the initial hypotheses (see [188] for a review). This phenomenon is widely used by metallurgists to control the grain size during the forming process of many alloys, including superalloys. Predictive tools are then needed to model accurately this phenomenon and thus optimize the final grain size and in-use properties of the materials. Classical laws predicting the limiting MGS [188], noted $\overline{R}_\infty$ have the following form:

$$\overline{R}_\infty = K\frac{\overline{r}}{f^m}, \tag{41}$$

where K and m are fitted parameters which can be assumed constant [188] or dependent of the material and/or the characteristics of the SPP population [188,119]. Since thirty years, numerous full-field modeling of the Smith-Zener phenomenon have been proposed, including Monte Carlo/Cellular Automata frameworks [189–194], front tracking or vertex [195,196], MPF [197–200] and LS [201,119,132,202,26,203,204].

In the LS framework, the concept of incorporating inert SPP within an FE framework was initially proposed for conducting 2D GG simulations [201] and 2D PDRX simulations [119] for the Inconel 718 alloy. SPPs are integrated into the FE mesh using statistical descriptions or experimental data, and the local curvature of the grain boundaries in contact with SPPs is constrained. This approach allows for the consideration of SPPs without assuming their size or morphology, and it accommodates isotropic and anisotropic particle/grain interface energies, whether they are incoherent or coherent interfaces. The effect of particle dragging is naturally captured by modifying the local curvature when the grain boundary encounters the particles, eliminating the need for explicit assumptions about the dragging pressure exerted by the particles.

Moreover, the Smith-Zener pinning effect induced by the presence of particles is naturally accounted for by imposing relevant boundary conditions at the interfaces between GBs and SPPs. Specifically, the influence of SPPs on microstructure evolution is considered by applying a Neumann-type limit condition on the GLS at the surface of the precipitates following the Young-Herring surface tension equilibrium:

$$\nabla\psi \cdot \mathbf{n} = sin\left(\alpha\right) = \frac{\gamma_p^2 - \gamma_p^1}{\gamma}, \tag{42}$$

where, as illustrated in Fig. 11, $\mathbf{n}$ is here the external unitary normal vector to the precipitate, α is the angle established by the balance of surface tensions at contact positions between the SPP and the grain boundary. So, when the particle is assumed incoherent with the matrix, $\gamma_p^1 \simeq \gamma_p^2$, which leads to $\alpha \simeq 0$, a null Neumann boundary condition is applied at the precipitate/grain boundary interface through the respect of Eq. (42).

This approach was used to support the idea that the phenomenon reported as abnormal grain growth in Inconel 718 could be explained by the growth of lower energy grains in a pinned microstructure and as such be a particular case of PDRX. Thanks to these

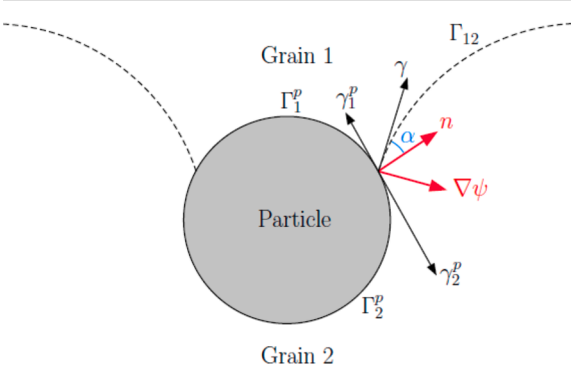

Fig. 11. 2D illustration of the interaction between a particle and a GB (dashed lines between Grain 1 and Grain 2). $\mathbf{n}$ corresponds to the normal to the particle interface, $\nabla\psi$ to the normal to the GB and α to the angle established by the balance of surface tensions. From [203,205].

simulations, the sensitivity of this phenomenon to the initial stored energy distribution could be studied [132]. Optimization of parameters K and m of Eq. 41 thanks to a full-field simulations campaign and first 3D LS simulations were proposed in [202,47], respectively. Comparisons with Monte Carlo simulations and experimental data have been made for ODS steels [26]. Fig. 12 illustrates a 3D GG LS simulations for Inconel 718 realized by Scholtes et al. [202] with an idealized spherical population of SPP (f = 3%), until reaching a final stable microstructure.

However, this initial LS approach for describing SPPs exhibits several limitations:

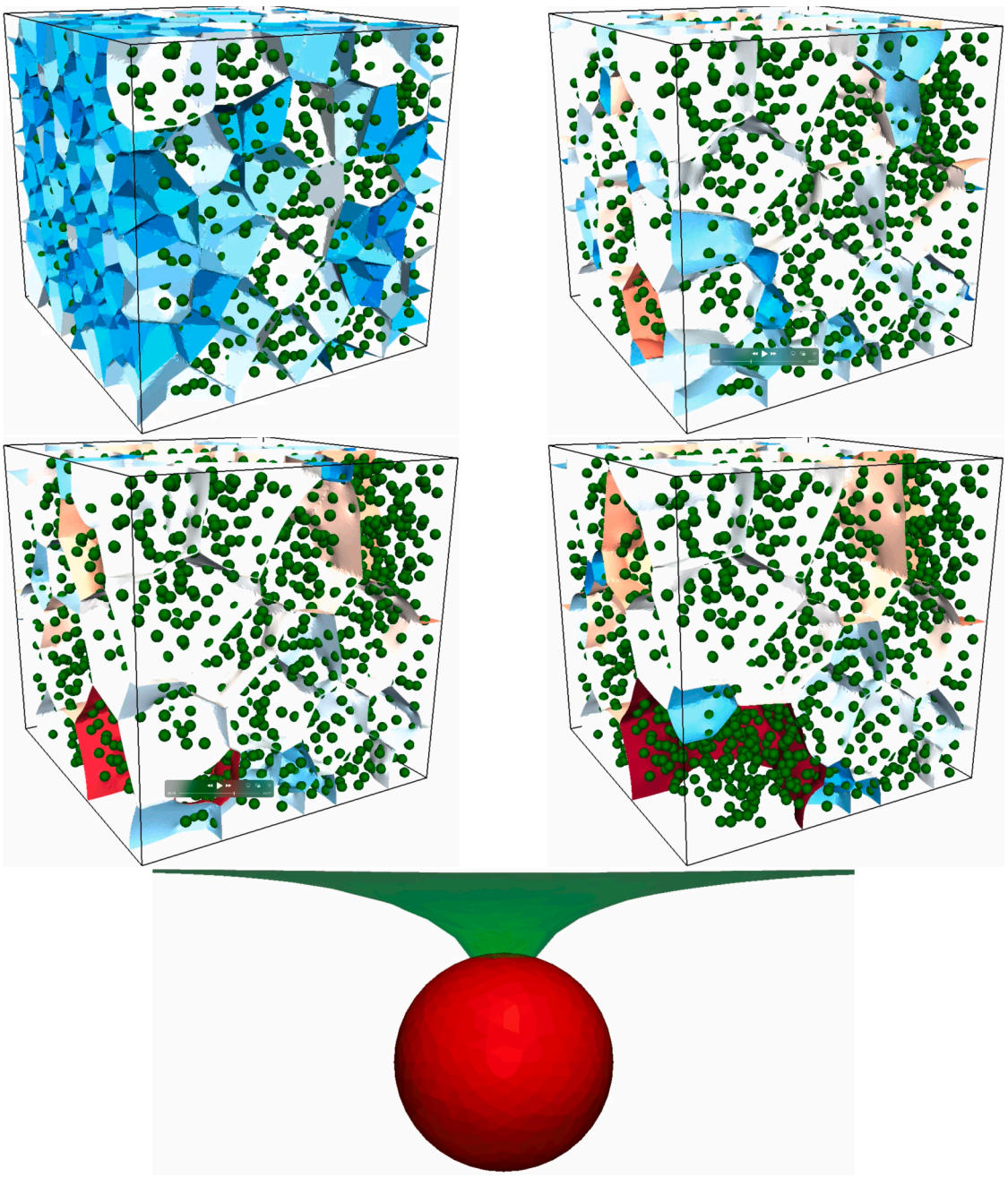

Fig. 12. 3D GG LS simulations for Inconel 718 with an idealized spherical population of SPP (f = 3%). SPP are described in green, the grain boundary network is described with a color code corresponding to the grain size until a stable configuration. From top to bottom and left to right: time evolution during the thermal treatment from the initial configuration to the stable grain boundary network. A video is available online. The last image corresponds to a zoom of a SPP (in red) interacting with one GB (in green) just before unpinning. A complete video is available online.

- Simulating material deformations is not straightforward when attempting to consider SPP behavior, as SPPs are not volumetrically described in the considered FE mesh,
- the aforementioned issue may become critical in the context of DDRX. It is widely recognized that the interfaces of SPPs serve as conducive sites for new grain formation. Therefore, a detailed representation of the mechanical fields at the SPP interfaces is essential,
- the simulation time can be significantly extended due to remeshing operations around particles and grain boundaries, mainly in 3D,
- the evolution of SPPs due to diffusive mechanisms—such as precipitation/dissolution, Ostwald Ripening, agglomeration, and spheroidization—cannot be accounted for, as SPPs are considered static in the current LS formulations.

For these reasons, a new LS approach to model ReX and GG mechanisms in presence of meshed SPPs and able to reproduce evolving particles was proposed by Alvarado et al. [203,204]. In this LS formulation, the description of SPPs is made by a new LS function, ψ_{SPP}, over the domain calculation without considering holes in the FE mesh. The GLS fields describing the grains are initially modified with simple topological operations (following by a reinitialization step) to introduce the presence of the SPPs, without modifying the particle interface:

$$\forall i \in [[1, N_{GLS}]] \quad \widehat{\psi}_i(\mathbf{x}, t=0) = min(\psi_i(\mathbf{x}, t=0), -\psi_{SPP}(\mathbf{x}, t=0)\,). \tag{43}$$

This operation is followed by a reinitialization procedure, $\psi_i(\mathbf{x}, t=0) = Redist(\widehat{\psi}_i(\mathbf{x}, t=0)\,)\forall i \in \{1, 2, \ldots, N_{GLS}\}$, as the resulting GLS functions are not (when the intersection is not empty) a distance function, even if GLS and ψ_{SPP} are. Of course, the function $\psi_{SPP}(\mathbf{x}, t=0)$ can be easily estimated as the distance function to the union of simple objects (as circles for spherical particles) but also obtained through the FE-immersion of an experimental map [119,47].

As already discussed (see Eq. (25)), the appearance of voids or overlaps especially at the multiple junctions after solving the convective-diffusive equations was first treated in [36] and implement in several cases, in 2D and 3D, using the LS method

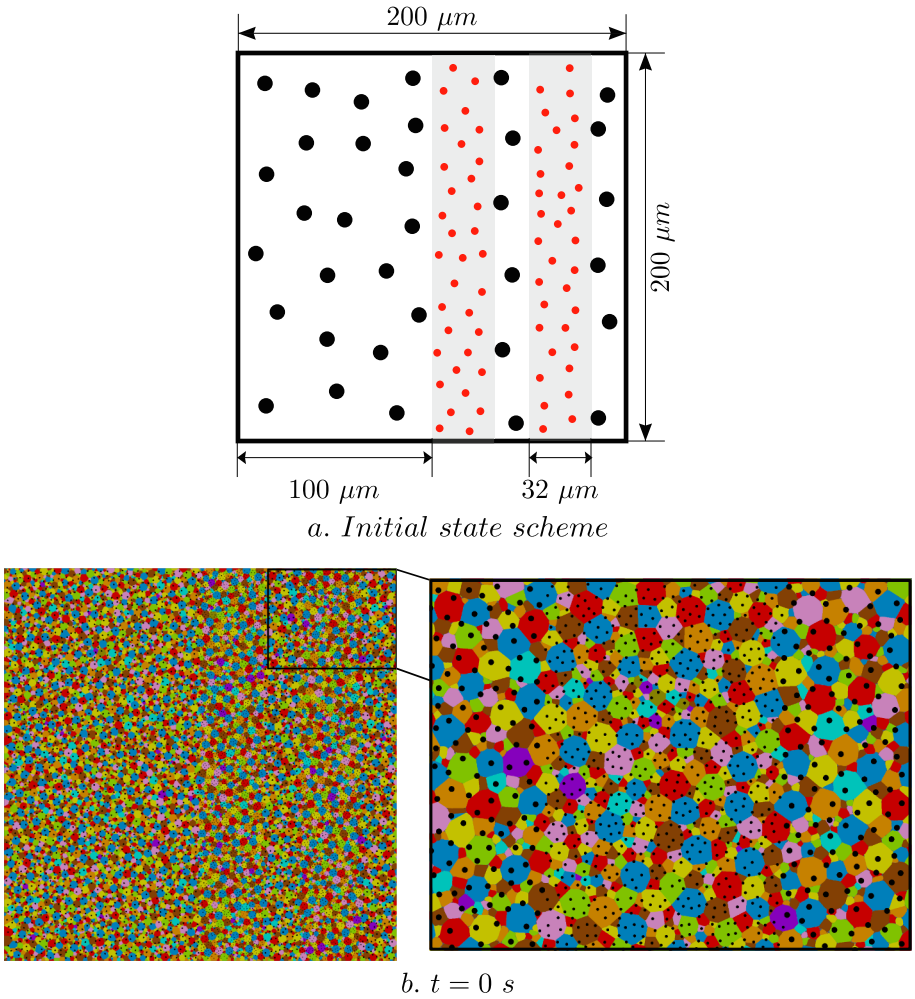

Fig. 13. Schematic and initial microstructure for a heterogeneous SPPs dispersion in a LS framework (SPPs are in black). From [203].

[47,45,134]. In order to respect the Young-Herring equilibrium without hollowing out the SPPs, this classical treatment is extended by taken into account ψ_{SPP} in the procedure:

$$\widehat{\psi}_i(\mathbf{x},t) = \frac{1}{2}\left(\psi_i(\mathbf{x},t) - \max\left(\max_{j\neq i}\left(\psi_j(\mathbf{x},t)\right), \psi_{SPP}(\mathbf{x},t)\right)\right), \quad \forall i \in \left\{1,2,\ldots,N_{GLS}\right\}, \quad \forall \mathbf{x} \in \Omega. \tag{44}$$

$$\psi_i(\mathbf{x},t) = \ Redist(\widehat{\psi}_i(\mathbf{x},t)) \quad \forall i \in \{1,2,\ldots,N_{GLS}\} \tag{45}$$

In the zones without SPPs, this methodology is equivalent to the classical numerical treatment (Eq. (25)) whereas when SPPs are present, it enables, by successive iterations, to impose the Young-Herring equilibrium for incoherent SPPs.

In real thermomechanical processes, which typically encompass significant temperature changes, it becomes crucial to model the evolution of SPPs. This modeling is key to quantitatively and qualitatively predicting the evolution of the microstructure, particularly with respect to grain size distribution. Hence, the ability to model the transformation of particles during GG is indispensable for managing actual industrial processes and forecasting microstructural evolution accurately.

In this LS framework, once the initial mesh is generated, the polycrystal can be created statistically or experimentally from an EBDS map. Subsequently, the grains fields ψ_i are adjusted to incorporate the new particles field ψ_{SPP}. The convective equation, Eq. (22), is then applied to ψ_{SPP}. This involves computing a velocity, v_{spp}, using prescribed data related to the time-dependent evolution of the particle's radius. Following this, a smoothed velocity field v is computed using Laplace's equation (see Eq. 46) with Dirichlet boundary conditions, v_{spp}, set at the particle interfaces, and null-Neumann boundary conditions applied to the boundaries of the domain. Finally v is used to compute the velocity field $\mathbf{v}$ oriented towards the center of each precipitate to be applied to ψ_{SPP} :

$$\begin{cases} \Delta v = 0 \\ v = v_{spp} \quad at \quad \Gamma_{spp} \\ \nabla v \cdot \mathbf{n} = 0 \quad at \quad \partial\Omega \backslash \Gamma_{spp} \end{cases} \tag{46}$$

and

$$\mathbf{v} = v\mathbf{n}_{SPP} = -v\nabla\psi_{SPP}, \tag{47}$$

with $\mathbf{n}$ the normal to the boundaries of the domain, $\mathbf{n}_{SPP}$ the unitary inside normal vector to the SPP, v_{spp} the velocity to impose to the SPPs and $\mathbf{v}$ the resulting velocity field which is really imposed, through a convection equation to ψ_{SPP}.

This methodology is illustrated in Figs. 13 and 14 where a simulation domain of 200x200 μm with an initial number of grains around 50000 is considered in context of $AD730^{TM}$ nickel base superalloy. The mean grain radius (in number) $\overline{R}$ is equal to 5μm and a spherical particles population, with an initial surface fraction $f_{spp} = 6\%$ divided in large SPPs with $f^1_{spp} = 4\%$ of radius $r^1_{spp} = 2\ \mu m$ and small SPPs with $f^2_{spp} = 2\%$ of radius $r^2_{spp} = 1\ \mu m$ distributed in two bands in the domain, is considered (as illustrated in Fig. 13.a).

Material properties and particle velocity v_{spp} for the chosen annealing temperature profile were obtained through experimental investigations [204]. The small particles are dissolved before the large particles, thus the bands regions present a classical GG mechanism sooner than the entire domain.

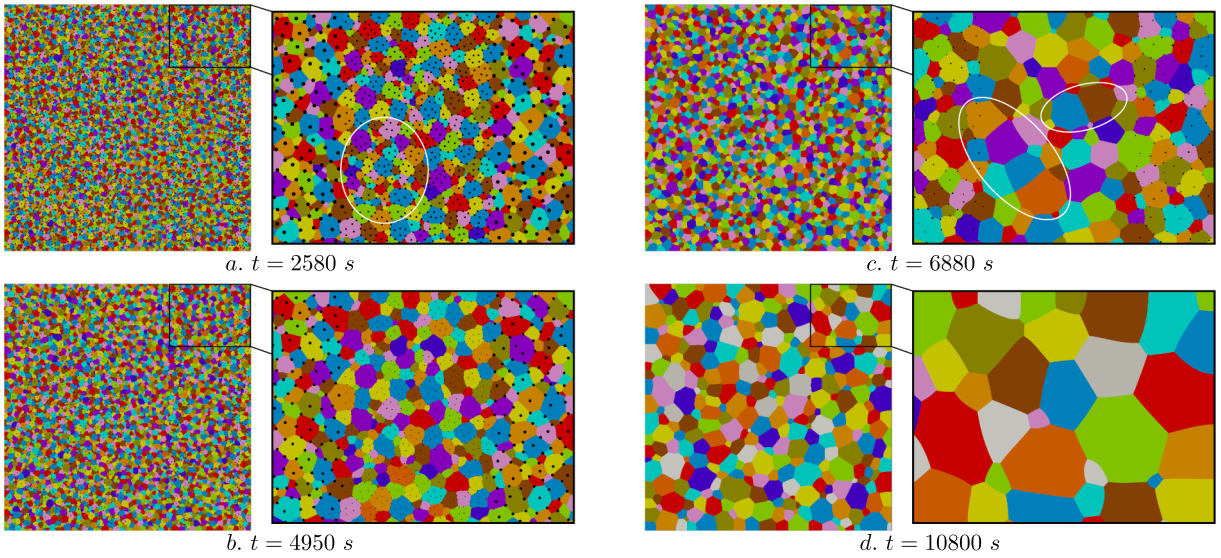

Fig. 14. Microstructure evolution at different times for a heterogeneous SPPs distribution (SPPs are in black). From [203]. A complete video is available online.

Fig. 14 from [203] illustrates the evolution of the microstructure at different stages of the simulation (2580s, 4950s, 6880s and 10800s) showing the particle and GG evolution during annealing.

For the initial isothermal treatment where the particles do not evolve, the grain size are smaller in the zones composed of small SPPs. This can be easily explained by a bigger resulting pinning pressure in this zone than in the zone with large SPPs (see Fig. 14.a). When the temperature increases, the particles begin to dissolve and the grains evolve, especially at the regions composed of small particles where the small grains of this regions begin to grow (see Fig. 14.b). Once the small SPPs are completely dissolved, the grains can grow freely and as represented in Fig. 14.c (white ellipses) some grains can grow more than others, thus a heterogeneous grain evolution begins to take place, where some grains are likely to grow more and more leading potentially to abnormal grain growth.

The thermal treatment ends with a maintain of temperature at 1120°C which is superior to the solvus temperature, so no particles remain and all the domain converge towards a classical GG mechanism as illustrated in Fig. 14.d.

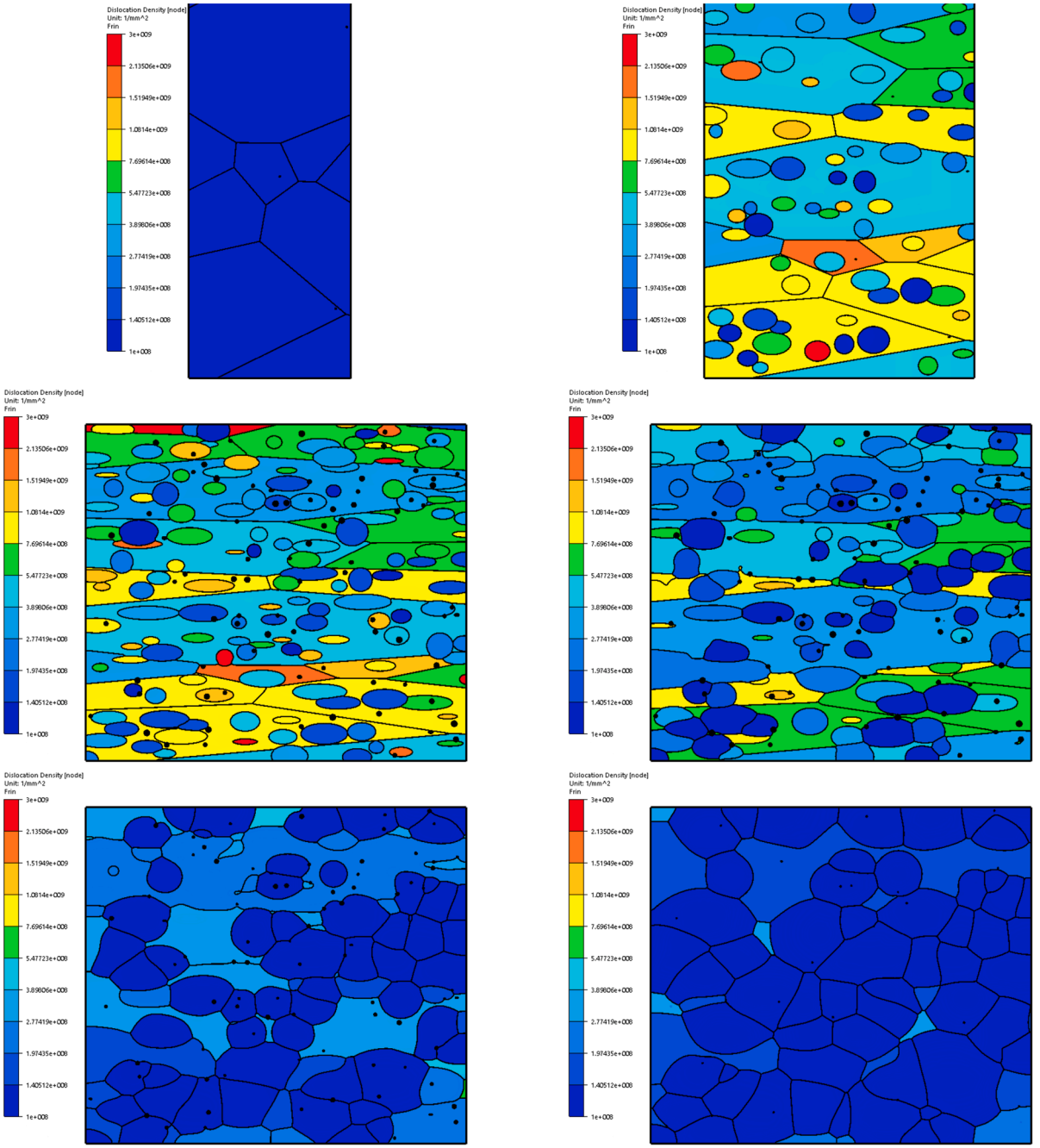

Fig. 15. Complex thermomechanical path for a Zirconium alloy. Time evolution of the microstructure thank to a LS modeling strategy, from [208].

This recent LS formalism opens also the possibility to simulate material deformations more naturally by taken into account the mechanical behavior of SPPs. Validation and comparisons of this proposed LS-FE numerical framework comparatively to previous formulations [119,47] and experimental data were proposed in [203,204], respectively.

Clearly, the various components presented earlier now allow to approach increasingly realistic complex thermomechanical paths for real materials. If Fig. 7 was a first example in context of 3D DDRX mechanism, the following illustration (Fig. 15), derived from the DIGIMU software package solution [206] based on the LS method [207,208,49,209], describes a deformation step of a zirconium alloy where CDRX mechanism occurs. Furthermore, the thermal path followed leads to the precipitation of a SPP population (black circles), affecting the migration of GB through Smith-Zener pinning. This population eventually dissolves when the temperature rises during the post-dynamic regime. This evolution, while reasonable in terms of the number of grains and SPP, remains extremely complex in terms of the considered mechanisms and incorporates all of the previously discussed numerical algorithms: Lagrangian deformation, continuous evolution of LAGB to HAGB with the consideration of GB property heterogeneities, along with the explicit modeling of the interaction between evolving GB and evolving particles, and post-dynamic evolutions.

A natural perspective of this illustration like another ones considered in this section will be to consider a more physics-based modeling for SPP precipitation, evolution and/or dissolution, likely utilizing the tools described in the following section.

7. Modeling of diffusive solid-state phase transformation

Until recently, the LS approach in the context of polycrystalline microstructure was primarily used for modeling ReX and related phenomena in single-phase materials. However, SSPT entails crystallographic changes in the parent phase, which occur through rearrangement of the lattice structure to form a different, more stable product phase, all while remaining in the same solid state. SSPT can either be displacive or diffusive. Displacive transformation [210] is characterized by spontaneous, coherent, and coordinated atomic movement over relatively short distances. On the other hand, diffusive transformation [211] involves a more gradual reorganization of the lattice through short and long-range atomic diffusion.

Two fundamental mechanisms drive diffusive SSPT: (i) the diffusion of solutes across phase interfaces and within the grain bulk, resulting in changes in chemical composition, and (ii) interface migration leading to lattice rearrangement or structural changes. Phase transformation plays a critical role in generating a range of materials with diverse microstructural characteristics during thermomechanical treatments.

In the context of diffusive SSPT, PFM have gained popularity and extensive usage due to their thermodynamic consistency and their ability to model complex morphological changes. The pioneering work of Wheeler et al. [212] and Steinbach et al. [31,213] on solidification using PFM laid some of the mathematical groundwork for phase-field modeling in multi-component, multi-phase systems involving solute diffusion. Despite this, the majority of existing numerical frameworks are primarily devoted to model ReX and GG in single-phase materials or to modeling phase transformations without considering ReX and associated phenomena. In light of this, a novel LS approach has recently been proposed to consider both aspects simultaneously [107].

Modeling diffusive SSPT at the mesoscopic scale typically necessitates two governing equations: a diffusion equation that regulates the distribution of solute atoms across different phases, and another equation that manages the migration of the resulting interface network. Traditionally, the diffusion equation can be resolved within a LS framework. However, the presence of material discontinuities at the phase interfaces requires explicit consideration of interface jump conditions when solving the diffusion equation in the LS framework. This requires the explicit localization of the interface at every moment to numerically manage the necessary jump conditions.

To circumvent this complex step, Chandrappa et al. [214,107] proposed considering a diffuse interface hypothesis across the phase interfaces during the resolution of the diffusion equation. In simpler terms, while the multi-phase grain interface network is migrated using an LS description, a global diffusion equation is considered based on a diffusive interface assumption for the phase interfaces. This approach allows for the resolution of a single diffusion equation throughout the entire computational domain, eliminating the need for any interface jump conditions.

The transition between a distance function to a diffuse interface description can be established, thanks to a hyperbolic tangent relation:

$$\phi(\mathbf{x},t) = \frac{1}{2} tanh\left(\frac{3\psi(\mathbf{x},t)}{\eta}\right) + \frac{1}{2}, \tag{48}$$

where η is a diffuse interface thickness parameter. In the following, we shall refer this function (ϕ) yielding the diffuse interface as the phase-field function. In the following, the particular case of austenite decomposition to ferrite by carbon diffusion is illustrated even if the framework can be generalized. the total carbon concentration field (C) can be expressed as a continuous variable as the solute flux:

$$C = \phi C_\alpha + (1-\phi) C_\gamma, \quad \boldsymbol{J} = \phi \boldsymbol{J}_\alpha + (1-\phi)\boldsymbol{J}_\gamma. \tag{49}$$

The diffuse phase interface is assumed to be composed of a mixture of the two phases. A constant concentration ratio between the phases is enforced. This stipulation ensures that the redistribution of solute atoms at the interface aligns with a partitioning ratio (denoted as k) equal to that at the equilibrium::

$$k = \frac{C_\alpha}{C_\gamma} = \frac{C_\alpha^{eq}}{C_\gamma^{eq}}, \tag{50}$$

where C_α^{eq} and C_γ^{eq} are the equilibrium concentrations of α and γ phases respectively at temperature T.

Following Fick's laws of diffusion, the diffusion equation for carbon partitioning can be expressed as:

$$\partial_t C = -\nabla\cdot\boldsymbol{J} = -\nabla\cdot\left[\phi\boldsymbol{J}_\alpha + (1-\phi)\boldsymbol{J}_\gamma\right],$$

with,

$$\boldsymbol{J}_\alpha = -D_\alpha^C\nabla C_\alpha; \quad \boldsymbol{J}_\gamma = -D_\gamma^C\nabla C_\gamma.$$

We then obtain,

$$\partial_t C = \nabla\cdot\left[\phi D_\alpha^C\nabla C_\alpha + \left(1-\phi\right)D_\gamma^C\nabla C_\gamma\right], \tag{51}$$

where D_α^C and D_γ^C represent the diffusivity of the carbon element in ferrite and austenite phases respectively.

Invoking eqs.(49) and (50) in eq.(51), a modified carbon diffusion equation [213] is obtained:

$$\partial_t C = \nabla\cdot\left(D^*\left(\phi\right)\left[\nabla C - \frac{C(k-1)}{1+\phi(k-1)}\nabla\phi\right]\right), \tag{52}$$

where $D^*(\phi)$ is called "mixed diffusivity" and is defined as,

$$D^*\left(\phi\right) = \frac{D_\gamma^C + \phi\left(kD_\alpha^C - D_\gamma^C\right)}{1+\phi(k-1)}.$$

With further simplifications, the above Eq.(52) can be transformed into a Convective-Diffusive-Reactive (CDR) form as follows:

$$\partial_t C = \nabla\cdot[D^*(\phi)\nabla C - C\boldsymbol{A}(\phi)]$$

$$\partial_t C + (\boldsymbol{A} - \nabla D^*)\cdot\nabla C - D^*\Delta C + RC = 0, \tag{53}$$

where,

$$\boldsymbol{A}\left(\phi\right) = \frac{D^*(\phi)(k-1)}{1+\phi(k-1)}\nabla\phi, \quad and \quad R = \nabla\cdot\boldsymbol{A}.$$

Interestingly, when applying the weak form of the prior equation in a FE resolution, the gradient of the mixed diffusivity term (∇D^*) vanishes. This aspect carries significant value with regard to numerical stability, especially considering the abrupt changes of this term across a phase interface.

Concerning interface migration, following Eq. 17, P can be defined as,

$$P = \Delta G + [\![E]\!] - \kappa\sigma. \tag{54}$$

The ΔG component acts only across the phase interfaces while vanishing across the grain interfaces of similar phases. Also, the sense and value of interface mobility, and interface energy could be different depending on the type of interface (i.e., α/γ phase interface, α/α grain interface, and the γ/γ grain interface). Eq. 30 can be then generalized in the following form:

$$\partial_t\psi_i + \left[\boldsymbol{v}_{\Delta G} + \boldsymbol{v}^{[\![\rho]\!]}\right]_i\cdot\nabla\psi_i - \left[\sum_{l\in\mathscr{S}}\chi_l\mu_l\sigma_l\right]\Delta\psi_i = 0 \qquad \forall i\in\left\{1,2,\ldots,N_{GLS}\right\}, \tag{55}$$

where $\mathscr{S} = \{\alpha\gamma,\alpha\alpha,\gamma\gamma\}$, $\boldsymbol{v}_{\Delta G} = \chi_{\alpha\gamma}\mu_{\alpha\gamma}\Delta G_{\alpha\gamma}\boldsymbol{n}$, and $\boldsymbol{v}^{[\![\rho]\!]} = \left[\sum_{l\in\mathscr{S}}\chi_l\mu_l[\![E]\!]_l\right]\boldsymbol{n}$.

As previously introduced, these equations must be followed by a multiple-junction treatment (Eq. 25 and a reinitialization step (Eq. 26). Moreover, as for $\boldsymbol{v}^{[\![\rho]\!]}$ (see Eq. 33), $\boldsymbol{v}_{\Delta G}$ component can be built as a unique function in the FE mesh:

$$\boldsymbol{v}_{\Delta G}\left(\begin{array}{c}\mathbf{x},t\end{array}\right) = \sum_{i=1}^{N_{GLS}}\sum_{\substack{j=1\\ j\neq i}}^{N_{GLS}}\chi_{G_i}\left(\begin{array}{c}\mathbf{x},t\end{array}\right)\mu_{ij}\exp\left(-\beta\left|\psi_j\left(\mathbf{x},t\right)\right|\right)\chi_{\alpha\gamma}\left(\begin{array}{c}\mathbf{x},t\end{array}\right)\Delta G_{\alpha\gamma}\mathscr{T}_s\left(\begin{array}{c}\mathbf{x},t\end{array}\right)\left(\begin{array}{c}-\boldsymbol{n}_j\end{array}\right), \tag{56}$$

where $\chi_{\alpha\gamma}$, as seen earlier, helps to filter this component of velocity field only on the phase interfaces and

$$\mathscr{T}_s\left(\mathbf{x},t\right) = \chi_\alpha\left(\mathbf{x},t\right) - \chi_\gamma\left(\mathbf{x},t\right) = 2\chi_\alpha\left(\mathbf{x},t\right) - 1, \tag{57}$$

with $\chi_\alpha(\mathbf{x},t)$ and $\chi_\gamma(\mathbf{x},t)$ the characteristic functions of α and γ phase, respectively.

The last ingredient missing to completely prescribe the above kinetics is the change in Gibbs free energy between the two phases. $\Delta G_{\alpha\gamma}$ is typically dependent on the local composition of the solutes, temperature, and the pressure. In many works, the description for $\Delta G_{\alpha\gamma}$ has been established by thermodynamic evaluations based on Calphad data [215] or ThermoCalc software [216]. For certain sharp interface descriptive models, the diffusion in the product phase is assumed to be instantaneous and so $\Delta G_{\alpha\gamma}$ is simply assumed to be proportional to the deviation in concentration at the interface in the parent phase ($C_{\gamma,eq}$) from the equilibrium concentration in this phase ($C_{\gamma,\gamma\alpha}$) [217,218]. In Chandrappa et al. [214,107] as in the works of Mecozzi [219], $\Delta G_{\alpha\gamma}$ is described based on a local linearization of the phase diagram and is basically assumed to be proportional to a small undercooling ($\Delta T = T^{eq} - T$). More details can be found in [107,214,73]. Fig. 16 (from [107]) illustrates the described numerical framework in a 2D case which corresponds to α phase nucleation and growth in a γ phase polycrystal.

8. Conclusion, limits, and perspectives

As highlighted, the level-set approach has spread extensively in computational metallurgy at the polycrystalline scale and is now used to model numerous mechanisms. The known advantages of this approach, explaining its relevance, primarily lie in its 'front-capturing' nature, where complex topological events (like the emergence and disappearance of grains) can be addressed in a completely natural way. Since the description of interfaces is not tied to a set of nodes and edges of the considered mesh or regular grid, the kinetics of the interfaces can thus be decoupled from that of the medium used for domain discretization. This strong point is, of course, common to multi-phase field type approaches. Moreover, if one take advantage of the allusion to multi phase-field approaches here to delve deeper. One can affirm that the level-set approach eliminates one of the inherent difficulties of phase field methods in defining, controlling, and optimizing the thickness to be considered in phase field approaches for a similar computational cost. The kinetic approach inherent to the LS method also negates the need to debate the comparative calibration of potential different Ginzburg–Landau functionals for the same mechanism.

Of course, if the level-set approach only had advantages, it would have spread much more in computational metallurgy compared to Monte Carlo, Cellular Automata or multi-phase field approaches, which are much more widely used in the community. This can easily be explained by the fact that each strong positive statement made in the previous paragraph can be offset by a negative argument. Let's try the exercise: While the front-capturing type description is often a sign of simplicity in topological events, it can also become a drawback when it comes to properly handling multiple junctions or when knowing their precise position and the neighboring discretization of the interfaces converging there can be indispensable for a rigorous consideration of the anisotropy of interface properties, as discussed in Section 5. This explains why this problem still remains stiff in all level-set formulations or multi-phase field approaches compared to vertex type approaches, for example. In regard to the link to the FE mesh, it is also useful to remember that while a discretization of the interface is not necessary, the precision of the interface description and its attributes remain however tied to the fineness of the mesh around the interfaces and/or the order of interpolation used. Therefore, it cannot be asserted, as is sometimes written, that the level-set description allows one to be completely independent from any work on the embedding FE mesh. Finally concerning the comparison with multi-phase field approach, it is probably useful to recall that the level-set framework can be seen somewhere as a particular extreme configuration of multi-phase field approach when a top hat potential is used as nicely depicted in the work of Steinbach [220]. The level-set approach brings precision in the description of the interface where the multi-phase field approach brings regularization of singularities at the interfaces.

Finally, in the author opinion, by taking into account the balance of the two previous paragraphs, the main interest of the level-set approach remains probably more in its versatility to take into account numerous mechanisms in a global numerical framework even in context of large deformation of the calculation domain. This likely explains its significance in modeling complex thermomechanical paths [48], and thus its unique potential for predicting microstructures in the context of hot metal forming processes [207,208,49,209]. On this matter, it seems evident to assert that level-set approaches are far from having demonstrated their full potential in the mechanisms that can be modeled. As presented in the previous section, solid-state transformations could become a new playground for these methods while taking into account the driving pressures also acting on grain boundaries. Other diffusion mechanisms are also within reach, such as surface diffusion [17]. The consideration of solute drag aspects at grain boundaries is also an area where the level-set approach could be improved to offer innovative solutions [221,222]. Finally, level-set approaches are also a powerful tool for accounting for all the mechanisms mentioned for processes related to powder metallurgy [223–225] where particles and their polycrystalline structures can be taken into account.

However, its main weakness, like other full-field approaches, lies in its high computational cost, mainly in 3D. In fact, if the goal here is to provide orders of magnitude for the computation times related to level-set simulations on FE meshes with remeshing algorithms on the latest generation CPUs, the following values can be suggested: In 2D, for a typical microstructure made of 1000 to 10,000 grains and no SPP, simulating a representative thermomechanical treatment can be achieved in a few hours on 8 CPUs. This computation time may extend to the range of a day to a few days when complex second-phase particle populations are present. In 3D, on 32 CPUs, these computation times can be extrapolated to days for simulations without second-phase particles and weeks for simulations with SPP. Such kind of discussions are provided in [86,109]. While these calculations are of interest in the modeling and understanding of mechanisms, their connection with component scale calculations remains very tenuous today due to the cost of these calculations and the necessity to have access to very large computing cluster if large calculation domains need to be investigated. The most advanced tools involve approaches where RVE simulations are conducted at a limited number of integration points within component-scale simulations. Thus, in R&D, low dimension/number of RVE and indirect coupling with component scale simulations

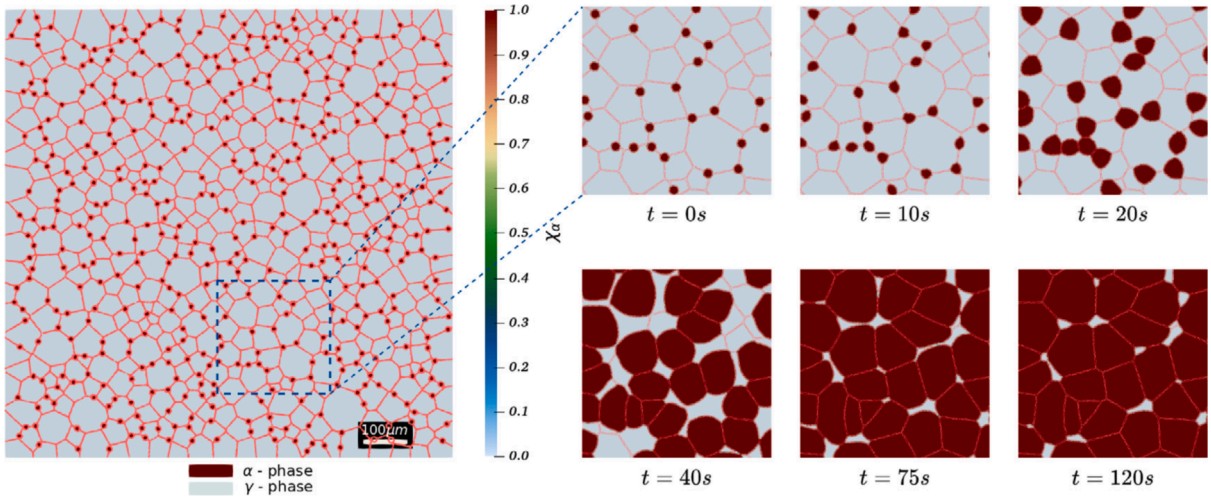

Fig. 16. α phase nucleation and growth in a γ phase polycrystal thanks to a LS-FE framework. From [107].

correspond to the more advanced tools. In this context, an evident perspective lies in the notable emergence of machine learning-trained surrogate models. These models, which are based entirely on artificial intelligence, serve as reduced order models derived from full-field simulations databases. Their primary advantage lies in their ability to offer predictive models at a significantly reduced computational cost [226–229]. Despite the evident appeal of these initial efforts, they are hindered by a few strong key limitations. Firstly, the representativeness of the training bases may be limited due to the inherent inaccuracies of the promoted full-field models. Secondly, the comparatively simplistic mechanisms primarily investigated thus far, such as grain growth and spinodal decomposition, do not adequately reflect the complexities found in actual metal forming conditions. Lastly, the considered microstructures lack the required intricacy, and hence may not provide an accurate representation of real materials. In context of hot metal forming, such nascent approaches are then currently unable to provide physically representative simulations at the mesoscopic scale. This constitutes, however, a very promising field in the coming years either for developing reduced order models, or even more intriguingly, to accelerate high-fidelity level-set simulations through mixed formulations (high-order time step resolution interposed with low-order ones) [228].

As highlighted, the representativity of Eq. 8 at the mesoscopic scale coupled to the usual 5D-space and models to described the grain boundary energy and mobility is more and more discussed and recent studies have resulted in contradictory conclusions on the subject. Indeed, the recent improvements of 3D grain growth and recrystallization experiments now make it possible to discuss in a much more precise way the veracity of this picture. Non-destructive in situ experiments allow to avoid bias inherent to 2D observations and open the path to precise reverse engineering of the $\| \nu \| / \kappa$ ratio. In this context, numerical reverse engineering by using anisotropic level-set formulations taken into-account the torque terms, will be of great interest to participate to this discussion.

Declaration of Competing Interest

The authors declare that they have no known competing financial interests or personal relationships that could have appeared to influence the work reported in this paper.

Data availability

Data will be made available on request.

Acknowledgement

The author extends deep gratitude to N. Bozzolo, R. Logé, Y. Chastel, P. De Micheli, A. Settefrati, A. Agnoli, K. Alvarado, N. Chandrappa, A.-L. Fabiano, J. Fausty, B. Flipon, S. Florez, V. Grand, K. Hitti, L. Maire, B. Murgas, B. Scholtes and M. Shakoor for all the discussions, exchanges, and results that have shaped many of the discussions and illustrations presented in this article. The author also sincerely thanks the DIGIMU consortium partners and the French Research National Agency (ANR), which, through the OPALE, DIGIMU, TOPAZE and RealIMotion Chairs (Grants No. ANR-14-CHIN-0002, ANR-16-CHIN-0001, ANR-19-CHIN-0005, and ANR-22-CHIN-0003), have contributed to some of these developments.

References

[1] Allison J, Cowles B, DeLoach J, Pollock T, Spanos G. Integrated computational materials engineering (ICME): implementing ICME in the aerospace, automotive, and maritime industries, A Study Organized by the Minerals, Metals & Materials Society. Miner, Metals Mater Soc, Warrendale, PA 2013;15086:9–10.
[2] Rollett A, Rohrer GS, Humphreys J. Recrystallization and related annealing phenomena, Amsterdam, Boston, Elsevier. 2017.
[3] Avrami M. Kinetics of phase change. i general theory. J Chem Phys 1939;7(12):1103–12.
[4] Kolmogorov AN. On the statistical theory of the crystallization of metals. Bull Acad Sci USSR, Math Ser 1937;1:355–9.
[5] Johnson W, Mehl R. Reaction kinetics in processes of nucleation and growth. Trans Am Inst Min Metall Petrol Eng 1939;195(416):416.
[6] Hillert M. On the theory of normal and abnormal grain growth. Acta Metall 1965;13(3):227–38. https://doi.org/10.1016/0001-6160(65)90200-2.
[7] Montheillet F, Lurdos O, Damamme G. A grain scale approach for modeling steady-state discontinuous dynamic recrystallization. Acta Mater 2009;57(5):1602–12.
[8] Cram D, Zurob H, Brechet Y, Hutchinson C. Modelling discontinuous dynamic recrystallization using a physically based model for nucleation. Acta Mater 2009;57(17):5218–28.
[9] Bernard P, Bag S, Huang K, Logé R. A two-site mean field model of discontinuous dynamic recrystallization. Mater Sci Eng: A 2011;528(24):7357–67.
[10] Maire L, Fausty J, Bernacki M, Bozzolo N, De Micheli P, Moussa C. A new topological approach for the mean field modeling of dynamic recrystallization. Mater Des 2018;146:194–207.
[11] Perez M, Dumont M, Acevedo-Reyes D. Implementation of classical nucleation and growth theories for precipitation. Acta Mater 2008;56(9):2119–32. https://doi.org/10.1016/j.actamat.2007.12.050.
[12] Seret A, Moussa C, Bernacki M, Bozzolo N. A mean field model of agglomeration as an extension to existing precipitation models. Acta Mater 2020;192:40–51. https://doi.org/10.1016/j.actamat.2020.04.029.
[13] Roth M, Flipon B, Bozzolo N, Bernacki M. Comparison of grain-growth mean-field models regarding predicted grain size distributions. Materials 2023;16(20).
[14] Miodownik M. A review of microstructural computer models used to simulate grain growth and recrystallisation in aluminium alloys. J Light Met 2002;2(3):125–35.
[15] Hallberg H. Approaches to modeling of recrystallization. Metals 2011;1(1):16–48.
[16] Militzer M. Phase field modeling of microstructure evolution in steels. Curr Opin Solid State Mater Sci 2011;15(3):106–15.
[17] Polychronopoulou D, Bozzolo N, Muñoz DP, Bruchon J, Shakoor M, Millet Y, Dumont C, von Thüngen IF, Besnard R, Bernacki M. Introduction to the level-set full field modeling of laths spheroidization phenomenon in α/β titanium alloys. Int J Mater Form 2019;12(2):173–83.
[18] Bruchon J, Pino Muñoz D, Valdivieso F, Drapier S, Pacquaut G. 3d simulation of the matter transport by surface diffusion within a level-set context. Eur J Comput Mech/Revue Européenne de Mécanique Numérique 2010;19(1–3):281–92.
[19] Rollett A, Srolovitz DJ, Doherty R, Anderson M. Computer simulation of recrystallization in non-uniformly deformed metals. Acta Metall 1989;37(2):627–39.
[20] Rollett AD, Manohar P. The Monte Carlo Method, John Wiley & Sons, Ltd; 2004, Ch. 4, pp. 77–114.
[21] Radhakrishnan B, Sarma G, Zacharia T. Monte carlo simulation of deformation substructure evolution during recrystallization. Scripta Mater 1998;39(12):1639–45.
[22] Radhakrishnan B, Sarma G, Zacharia T. Modeling the kinetics and microstructural evolution during static recrystallization—monte carlo simulation of recrystallization. Acta Mater 1998;46(12):4415–33.
[23] Zhang L, Rollett AD, Bartel T, Wu D, Lusk MT. A calibrated monte carlo approach to quantify the impacts of misorientation and different driving forces on texture development. Acta Mater 2012;60(3):1201–10.
[24] Wang W, Helbert A, Brisset F, Mathon M, Baudin T. Monte carlo simulation of primary recrystallization and annealing twinning. Acta Mater 2014;81:457–68.
[25] Sieradzki L, Madej L. A perceptive comparison of the cellular automata and Monte Carlo techniques in application to static recrystallization modeling in polycrystalline materials. Comput Mater Sci 2013;67:156–73.
[26] Villaret F, Hary B, de Carlan Y, Baudin T, Logé R, Maire L, Bernacki M. Probabilistic and deterministic full field approaches to simulate recrystallization in ODS steels. Comput Mater Sci 2020;179:109646.
[27] Raabe D. Cellular automata in materials science with particular reference to recrystallization simulation. Annu Rev Mater Res 2002;32(1):53–76.
[28] Janssens K. An introductory review of cellular automata modeling of moving grain boundaries in polycrystalline materials. Math Comput Simul 2010;80(7):1361–81.
[29] Golab R, Sitko M, Szyndler J, Madej L. Cellular automata finite element approach for modelling microstructure evolution under thermo-mechanical processing conditions. In: Cellular Automata. Lect. Notes Comput. Sci., Vol. 8751. Springer International Publishing; 2014. p. 197–207.
[30] Madej L, Sitko M. Computationally efficient cellular automata-based full-field models of static recrystallization: A perspective review. Steel Res Int 2023;94(3):2200657.
[31] Steinbach I, Pezzolla F, Nestler B, Seesselberg M, Prieler R, Rezende J. A phase field concept for multiphase systems. Physica D 1996;94:135–47.
[32] Moelans N, Blanpain B, Wollants P. Quantitative analysis of grain boundary properties in a generalized phase field model for grain growth in anisotropic systems. Phys Rev B 2008;78(2):024113.
[33] Krill III C, Chen L. Computer simulation of 3-D grain growth using a phase-field model. Acta Mater 2002;50(12):3059–75.
[34] Barrales Mora L, Gottstein G, Shvindlerman L. Three-dimensional grain growth: analytical approaches and computer simulations. Acta Mater 2008;56(20):5915–26.
[35] Florez S, Alvarado K, Muñoz DP, Bernacki M. A novel highly efficient lagrangian model for massively multidomain simulation applied to microstructural evolutions. Comput Methods Appl Mech Eng 2020;367:113107.
[36] Merriman B, Bence J, Osher S. Motion of multiple junctions: A level set approach. J Comput Phys 1994;112:334–63.
[37] Zhao H, Chan T, Merriman B, Osher S. A variational level set approach to multiphase motion. J Comput Phys 1996;127:179–95.
[38] Bernacki M, Chastel Y, Coupez T, Logé R. Level set framework for the numerical modelling of primary recrystallization in polycrystalline materials. Scripta Mater 2008;58(12):1129–32.
[39] Hallberg H, Bulatov VV. Modeling of grain growth under fully anisotropic grain boundary energy. Modell Simul Mater Sci Eng 2019;27(4):045002.
[40] Jin Y, Bozzolo N, Rollett A, Bernacki M. 2D finite element modeling of anisotropic grain growth in polycrystalline materials: level set versus multi-phase-field method. Comput Mater Sci 2015;104(15):108–23.
[41] Elsey M, Esedoglu S, Smereka P. Diffusion generated motion for grain growth in two and three dimensions. J Comput Phys 2009;21:8015–33.
[42] Mießen C, Liesenjohann M, Barrales-Mora L, Shvindlerman L, Gottstein G. An advanced level set approach to grain growth–accounting for grain boundary anisotropy and finite triple junction mobility. Acta Mater 2015;99:39–48.
[43] Elsey M, Esedoglu S, Smereka P. Large-scale simulation of normal grain growth via diffusion-generated motion. Proc R Soc A. 2011;467:381–401.
[44] Logé R, Bernacki M, Resk H, Delannay L, Digonnet H, Chastel Y, Coupez T. Linking plastic deformation to recrystallization in metals using digital microstructures. Phil Mag 2008;30–32:3691–712.
[45] Bernacki M, Logé R, Coupez T. Level set framework for the finite-element modelling of recrystallization and grain growth in polycrystalline materials. Scripta Mater 2011;64(6):525–8.
[46] Hallberg H, Ristinmaa M. Microstructure evolution influenced by dislocation density gradients modeled in a reaction-diffusion-system. Comput Mater Sci 2013;67:373–83.
[47] Scholtes B, Boulais-Sinou R, Settefrati A, Muñoz DP, Poitrault I, Montouchet A, Bozzolo N, Bernacki M. 3d level set modeling of static recrystallization considering stored energy fields. Comput Mater Sci 2016;122:57–71.
[48] Maire L, Scholtes B, Moussa C, Bozzolo N, Muñoz DP, Settefrati A, Bernacki M. Modeling of dynamic and post-dynamic recrystallization by coupling a full field approach to phenomenological laws. Mater Des 2017;133:498–519.

[49] P. De Micheli, K. Alvarado, V. Grand, M. Bernacki, Full field grain size prediction considering precipitates evolution and continuous dynamic recrystallization with DIGIMU solution, in: Proceedings of the 14th International Conference on the Technology of Plasticity - Current Trends in the Technology of Plasticity, Springer Nature Switzerland, 2024, pp. 563–574.
[50] Morawiec A. Orientations and rotations. Springer; 2003.
[51] Gurtin ME. Multiphase thermomechanics with interfacial structure 1. heat conduction and the capillary balance law. Arch Ration Mech Anal 1988;104(3):195–221.
[52] Gurtin ME. Toward a nonequilibrium thermodynamics of two-phase materials. Arch Ration Mech Anal 1988;100:275–312.
[53] Gurtin ME, Struthers A. Multiphase thermomechanics with interfacial structure: 3. evolving phase boundaries in the presence of bulk deformation. Arch Ration Mech Anal 1990;112:97–160.
[54] do Carmo MP. Differential geometry of curves and surfaces, Englewood Cliffs, New Jersey; 1976.
[55] Herring C. Surface tension as a motivation for sintering, Fundamental contributions to the continuum theory of evolving phase interfaces in solids: a collection of reprints of 14 seminal papers; 1999. p. 33–69.
[56] Abdeljawad F, Foiles SM, Moore AP, Hinkle AR, Barr CM, Heckman NM, Hattar K, Boyce BL. The role of the interface stiffness tensor on grain boundary dynamics. Acta Mater 2018;158:440–53.
[57] Du D, Zhang H, Srolovitz DJ. Properties and determination of the interface stiffness. Acta Mater 2007;55(2):467–71.
[58] K. Chen, J. Han, X. Pan, D.J. Srolovitz, The grain boundary mobility tensor, Proceedings of the National Academy of Sciences 117 (9) (2020) 4533–4538. doi:10.1073/pnas.1920504117.
[59] Bhattacharya A, Shen Y-F, Hefferan CM, Li SF, Lind J, Suter RM, Krill CE, Rohrer GS. Grain boundary velocity and curvature are not correlated in ni polycrystals. Science 2021;374(6564):189–93. https://doi.org/10.1126/science.abj3210.
[60] Xu Z, Hefferan CM, Li SF, Lind J, Suter RM, Abdeljawad F, Rohrer GS. Energy dissipation by grain boundary replacement during grain growth. Scripta Mater. 2023;230:115405. https://doi.org/10.1016/j.scriptamat.2023.115405.
[61] Florez S, Alvarado K, Murgas B, Bozzolo N, Chatain D, Krill CE, Wang M, Rohrer GS, Bernacki M. Statistical behaviour of interfaces subjected to curvature flow and torque effects applied to microstructural evolutions. Acta Mater 2022;222:117459.
[62] Laasraoui A, Jonas J. Prediction of steel flow stresses at high temperatures and strain rates. Metall. Trans. A 1991;22(7):1545–58. https://doi.org/10.1007/BF02667368.
[63] Kocks UF. Laws for Work-Hardening and Low-Temperature Creep. J. Eng. Mater. Technol. 1976;98(1):76–85. https://doi.org/10.1115/1.3443340.
[64] Mecking H, Kocks UF. Kinetics of flow and strain-hardening. Acta Metall. 1981;29(11):1865–75. https://doi.org/10.1016/0001-6160(81)90112-7.
[65] Cuitino AM, Ortiz M. Computational modelling of single crystals. Modell. Simul. Mater. Sci. Eng. 1993;1(3):225.
[66] Marin E, Dawson P. On modelling the elasto-viscoplastic response of metals using polycrystal plasticity. Comput. Methods Appl. Mech. Eng. 1998;165(1):1–21. https://doi.org/10.1016/S0045-7825(98)00034-6.
[67] Asaro R, Needleman A. Overview no. 42 texture development and strain hardening in rate dependent polycrystals. Acta Metall 1985;33(6):923–53.
[68] Wakai F, Brakke K. Mechanics of sintering for coupled grain boundary and surface diffusion. Acta Mater 2011;59(14):5379–87.
[69] A. Dervieux, F. Thomasset, A finite element method for the simulation of a rayleigh-taylor instability, in: Approximation Methods for Navier-Stokes Problems: Proceedings of the Symposium Held by the International Union of Theoretical and Applied Mechanics (IUTAM) at the University of Paderborn, Germany, September 9–15, 1979, Springer, 2006, pp. 145–158.
[70] Osher S, Sethian J. Fronts propagating with curvature-dependent speed: Algorithms based on Hamilton-Jacobi formulations. J. Comput. Phys. 1988;79(1):12–49.
[71] F.A. Williams, 3. Turbulent Combustion, pp. 97–131. doi:10.1137/1.9781611971064.ch3.
[72] Kerstein AR, Ashurst WT, Williams FA. Field equation for interface propagation in an unsteady homogeneous flow field. Phys. Rev. A 1988;37:2728–31. https://doi.org/10.1103/PhysRevA.37.2728.
[73] N. Chandrappa, A level-set formulation to simulate diffusive solid-state phase transformation in polycrystalline metallic materials, Ph.D. thesis, MINES Paris PSL (2024).
[74] Rollett AD, Saylor D, Fridy J, El-Dasher BS, Brahme A, Lee S, Cornwell C, Noack R. Modeling polycrystalline microstructures in 3d. AIP Conf. Proc. 2004;712(1):71–7.
[75] Xu T, Li M. Topological and statistical properties of a constrained voronoi tessellation. Phil. Mag. 2009;89(4):349–74.
[76] Imai H, Iri M, Murota K. Voronoi diagram in the laguerre geometry and its applications. SIAM J. Comput. 1985;14(1):93–105.
[77] Jodrey WS, Tory EM. Computer simulation of close random packing of equal spheres. Phys. Rev. A 1985;32:2347–51.
[78] He D, Ekere NN, Cai L. Computer simulation of random packing of unequal particles. Phys. Rev. E 1999;60:7098–104.
[79] Benabbou A, Borouchaki H, Laug P, Lu J. Geometrical modeling of granular structures in two and three dimensions. application to nanostructures. Int. J. Numer. Meth. Eng. 2009;80(4):425–54.
[80] Bagi K. A quasi-static numerical model for micro-level analysis of granular assemblies. Mech. Mater. 1993;16(1):101–10.
[81] Hitti K, Laure P, Coupez T, Silva L, Bernacki M. Precise generation of complex statistical Representative Volume Elements (RVEs) in a finite element context. Comput. Mater. Sci. 2012;61:224–38.
[82] Ilin, Dmitrii N., Bernacki, Marc, A new algorithm for dense ellipse packing and polygonal structures generation in context of fem or dem, MATEC Web Conf. 80 (2016) 02004. doi:10.1051/matecconf/20168002004.
[83] Ilin Dmitrii N, Bernacki Marc. Advancing layer algorithm of dense ellipse packing for generating statistically equivalent polygonal structures. Granular Matter 2016;18(3).
[84] Quey R, Renversade L. Optimal polyhedral description of 3D polycrystals: Method and application to statistical and synchrotron X-ray diffraction data. Comput. Methods Appl. Mech. Eng. 2018;330:308–33.
[85] Depriester D, Kubler R. Radical voronoï tessellation from random pack of polydisperse spheres: Prediction of the cells' size distribution. Comput. Aided Des. 2019;107:37–49.
[86] Scholtes B. Development of an efficient level set framework for the full field modeling recrystallization in 3D. MINES Paris PSL; 2016. Ph.D. thesis.
[87] K. Hitti, Direct numerical simulation of complex representative volume elements (RVEs): Generation, resolution and homogenization, Ph.D. thesis, MINES Paris PSL (2011).
[88] Mackenzie JK. Second paper on statistics associated with the random disorientation of cubes. Biometrika 1958;45(1–2):229–40. https://doi.org/10.1093/biomet/45.1-2.229.
[89] Cruz-Fabiano A-L, Logé R, Bernacki M. Assessment of simplified 2D grain growth models from numerical experiments based on a level set framework. Comput. Mater. Sci. 2014;92:305–12. https://doi.org/10.1016/j.commatsci.2014.05.060.
[90] Scholtes B, Shakoor M, Settefrati A, Bouchard P-O, Bozzolo N, Bernacki M. New finite element developments for the full field modeling of microstructural evolutions using the level-set method. Comput. Mater. Sci. 2015;109:388–98.
[91] R.I. Saye, J.A. Sethian, The voronoi implicit interface method for computing multiphase physics, Proceedings of the National Academy of Sciences 108 (49) (2011) 19498–19503. doi:10.1073/pnas.1111557108.
[92] Quey R, Dawson P, Barbe F. Large-scale 3D random polycrystals for the finite element method: Generation, meshing and remeshing. Comput. Methods Appl. Mech. Eng. 2011;200(17–20):1729–45.
[93] Ludwig W, King A, Reischig P, Herbig M, Lauridsen EM, Schmidt S, Proudhon H, Forest S, Cloetens P, du Roscoat SR, Buffière JY, Marrow TJ, Poulsen HF. New opportunities for 3d materials science of polycrystalline materials at the micrometre lengthscale by combined use of x-ray diffraction and x-ray imaging. Materials Science and Engineering: A 2009;524(1):69–76.
[94] Proudhon H, Li J, Reischig P, Gueninchault N, Forest S, Ludwig W. Coupling diffraction contrast tomography with the finite element method. Adv. Eng. Mater. 2016;18(6):903–12.

[95] Young P, Beresford-West T, Coward S, Notarberardino B, Walker B, Abdul-Aziz A. An efficient approach to converting three-dimensional image data into highly accurate computational models. Philosophical Transactions of the Royal Society A: Mathematical, Physical and Engineering Sciences 2008;366(1878):3155–73.
[96] Zhang Y, Bajaj C, Sohn B-S. 3d finite element meshing from imaging data. Comput. Methods Appl. Mech. Eng. 2005;194(48):5083–106.
[97] Brahme A, Alvi MH, Saylor D, Fridy J, Rollett AD. 3d reconstruction of microstructure in a commercial purity aluminum. Scripta Mater. 2006;55(1):75–80.
[98] Sinchuk Y, Shishkina O, Gueguen M, Signor L, Nadot-Martin C, Trumel H, Van Paepegem W. X-ray CT based multi-layer unit cell modeling of carbon fiber-reinforced textile composites: Segmentation, meshing and elastic property homogenization. Compos. Struct. 2022;298:116003. https://doi.org/10.1016/j.compstruct.2022.116003.
[99] Bernacki M, Resk H, Coupez T, Logé R. Finite element model of primary recrystallization in polycrystalline aggregates using a level set framework. Modell. Simul. Mater. Sci. Eng. 2009;6:064006.
[100] Gruau C, Coupez T. 3D tetrahedral, unstructured and anisotropic mesh generation with adaptation to natural and multidomain metric. Comput. Methods Appl. Mech. Eng. 2005;194(48–49):4951–76.
[101] Coupez T, Digonnet H, Ducloux R. Parallel meshing and remeshing. Appl. Math. Model. 2000;25(2):153–75.
[102] Shakoor M, Bernacki M, Bouchard P-O. A new body-fitted immersed volume method for the modeling of ductile fracture at the microscale: Analysis of void clusters and stress state effects on coalescence. Eng. Fract. Mech. 2015;147:398–417.
[103] Almeida RC, Feijoo RA, Galeao AC, Padra C, Silva RS. Adaptive finite element computational fluid dynamics using an anisotropic error estimator. Comput. Methods Appl. Mech. Eng. 2000;182(3):379–400.
[104] Coupez T. Metric construction by length distribution tensor and edge based error for anisotropic adaptive meshing. J. Comput. Phys. 2011;230(7):2391–405.
[105] Mesri Y, Khalloufi M, Hachem E. On optimal simplicial 3D meshes for minimizing the hessian-based errors. Applied Numerical Mathematics 2016;109:235–49. https://doi.org/10.1016/j.apnum.2016.07.007.
[106] Maire L, Scholtes B, Moussa C, Bozzolo N, Pino Muñoz D, Bernacki M. Improvement of 3D mean field models for capillarity-driven grain growth based on full field simulations. J. Mater. Sci. 2016;51(24):10970–81.
[107] Chandrappa N, Bernacki M. A level-set formulation to simulate diffusive solid/solid phase transformation in polycrystalline metallic materials - application to austenite decomposition in steels. Comput. Mater. Sci. 2023;216:111840.
[108] Fausty J, Bozzolo N, Muñoz DP, Bernacki M. A novel level-set finite element formulation for grain growth with heterogeneous grain boundary energies. Materials & Design 2018;160:578–90.
[109] Florez S, Shakoor M, Toulorge T, Bernacki M. A new finite element strategy to simulate microstructural evolutions. Comput. Mater. Sci. 2020;172:109335.
[110] Sethian JA. Theory, algorithms, and applications of level set methods for propagating interfaces. Acta numerica 1996;5:309–95.
[111] Helmsen JJ, Puckett EG, Colella P, Dorr M. Two new methods for simulating photolithography development in 3d. In: Optical Microlithography IX, Vol. 2726. SPIE; 1996. p. 253–61.
[112] Tsitsiklis J. Efficient algorithms for globally optimal trajectories. IEEE Trans. Autom. Control 1995;40(9):1528–38. https://doi.org/10.1109/9.412624.
[113] Kimmel R, Sethian J. Computing geodesic paths on manifolds. Proc. Natl. Acad. Sci. USA 1998;95(15):8431–5.
[114] J.A. Sethian, A. Vladimirsky, Ordered upwind methods for static hamilton-jacobi equations: Theory and algorithms, Proceedings of the National Academy of Sciences of the United States of America 98 20 (2003) 11069–74.
[115] Adalsteinsson D, Sethian JA. The fast construction of extension velocities in level set methods. J. Comput. Phys. 1999;148(1):2–22.
[116] Zhao H. A fast sweeping method for eikonal equations. Mathematics of computation 2005;74(250):603–27.
[117] Tsai Y-HR, Cheng L-T, Osher S, Zhao H-K. Fast sweeping algorithms for a class of hamilton–jacobi equations. SIAM Journal on Numerical Analysis 2003;41(2):673–94. https://doi.org/10.1137/S0036142901396533.
[118] Sussman M, Smereka P, Osher S. A level set approach for computing solutions to incompressible two-phase flow. J. Comput. Phys. 1994;114:146–59.
[119] Agnoli A, Bozzolo N, Logé R, Franchet J-M, Laigo J, Bernacki M. Development of a level set methodology to simulate grain growth in the presence of real secondary phase particles and stored energy – Application to a nickel-base superalloy. Comput. Mater. Sci. 2014;89:233–41.
[120] Coupez T. Convection of local level set function for moving surfaces and interfaces in forming flow. AIP Conf. Proc. 2007;908(1):61–6.
[121] Elias R, Martins M, Coutinho A. Simple finite element-based computation of distance functions in unstructured grids. Internation journal for numerical methods in engineering 2007;72:1095–110.
[122] Jones M, Baerentzen J, Sramek M. 3d distance fields: a survey of techniques and applications. IEEE Trans. Visual Comput. Graphics 2006;12(4):581–99.
[123] Fortmeier O, Martin Bücker H. Parallel re-initialization of level set functions on distributed unstructured tetrahedral grids. J. Comput. Phys. 2011;230(12):4437–53.
[124] Shakoor M, Scholtes B, Bouchard P-O, Bernacki M. An efficient and parallel level set reinitialization method – application to micromechanics and microstructural evolutions. Appl. Math. Model. 2015;39(23):7291–302.
[125] Esedoglu S, Ruuth S, Tsai R. Diffusion generated motion using signed distance functions. J. Comput. Phys. 2010;229(4):1017–42.
[126] Elsey M, Esedog S, Smereka P, et al. Simulations of anisotropic grain growth: Efficient algorithms and misorientation distributions. Acta materialia 2013;61(6):2033–43.
[127] Mießen C, Velinov N, Gottstein G, Barrales-Mora LA. A highly efficient 3d level-set grain growth algorithm tailored for ccnuma architecture. Modell. Simul. Mater. Sci. Eng. 2017;25(8):084002.
[128] Saye R, Sethian J. Analysis and applications of the voronoi implicit interface method. J. Comput. Phys. 2012;231(18):6051–85. https://doi.org/10.1016/j.jcp.2012.04.004.
[129] Zaitzeff A, Esedoglu S, Garikipati K. On the voronoi implicit interface method. SIAM Journal on Scientific Computing 2019;41(4):A2407–29. https://doi.org/10.1137/18M1222569.
[130] Ruiz D, Pino Muñoz D, Bernacki M. A new numerical framework for the full field modeling of dynamic recrystallization in a CPFEM context. Comput. Mater. Sci. 2020;179:109645.
[131] Ruiz D, Bozzolo N, Moussa C, Maire L, Pino Muñoz D, Bernacki M. Full field modeling of dynamic recrystallization in a CPFEM context - application to 304L steel. Comput. Mater. Sci. 2020;184:109892.
[132] Agnoli A, Bernacki M, Logé R, Franchet J-M, Laigo J, Bozzolo N. Selective growth of low stored energy grains during δ sub-solvus annealing in the inconel 718 nickel base superalloy. Metallurgical and Materials Transactions A 2015;46(9):4405–21.
[133] Grand V, Flipon B, Gaillac A, Bernacki M. Characterization and modeling of the influence of initial microstructure on recrystallization of zircaloy-4 during hot forming 2022;arXiv (2203.08447).
[134] Ilin D, Bozzolo N, Toulorge T, Bernacki M. Full field modeling of recrystallization: Effect of intragranular strain gradients on grain boundary shape and kinetics. Comput. Mater. Sci. 2018;150:149–61.
[135] Grand V, Flipon B, Gaillac A, Bernacki M. Modeling cdrx and mdrx during hot forming of zircaloy-4. Modell. Simul. Mater. Sci. Eng. 2023;31(8):085008. https://doi.org/10.1088/1361-651X/acfe27.
[136] Smith CS. Introduction to grains, phases, and interfaces—an interpretation of microstructure. Transactions of the American Institute of Mining and Metallurgical Engineers 1948;175(2):15–51.
[137] Kohara S, Parthasarathi MN, Beck PA. Anisotropy of boundary mobility. J. Appl. Phys. 1958;29(7):1125–6.
[138] Anderson M, Srolovitz D, Grest G, Sahni P. Computer simulation of grain growth—i. kinetics. Acta Metall 1984;32(5):783–91.
[139] Gao J, Thompson R. Real time-temperature models for monte carlo simulations of normal grain growth. Acta materialia 1996;44(11):4565–70.
[140] Lazar EA, Mason JK, MacPherson RD, Srolovitz DJ. A more accurate three-dimensional grain growth algorithm. Acta Mater 2011;59(17):6837–47.
[141] Garcke H, Nestler B, Stoth B. A multiphase field concept: numerical simulations of moving phase boundaries and multiple junctions. SIAM Journal on Applied Mathematics 1999;60(1):295–315.

[142] Rollett A, Srolovitz DJ, Anderson M. Simulation and theory of abnormal grain growth—anisotropic grain boundary energies and mobilities. Acta Metall 1989;37(4):1227–40.
[143] Hwang NM. Simulation of the effect of anisotropic grain boundary mobility and energy on abnormal grain growth. Journal of materials science 1998;33(23):5625–9.
[144] Upmanyu M, Hassold GN, Kazaryan A, Holm EA, Wang Y, Patton B, Srolovitz DJ. Boundary mobility and energy anisotropy effects on microstructural evolution during grain growth. Interface Sci. 2002;10(2–3):201–16.
[145] Zöllner D, Zlotnikov I. Texture controlled grain growth in thin films studied by 3d potts model. Advanced Theory and Simulations 2019;2(8):1900064.
[146] Miyoshi E, Takaki T. Validation of a novel higher-order multi-phase-field model for grain-growth simulations using anisotropic grain-boundary properties. Comput. Mater. Sci. 2016;112:44–51.
[147] Chang K, Chang H. Effect of grain boundary energy anisotropy in 2D and 3D grain growth process. Results in Physics 2019;12:1262–8.
[148] Miyoshi E, Takaki T, Ohno M, Shibuta Y. Accuracy evaluation of phase-field models for grain growth simulation with anisotropic grain boundary properties. ISIJ Int. 2019 ISIJINT–2019.
[149] Fausty J, Bozzolo N, Bernacki M. A 2d level set finite element grain coarsening study with heterogeneous grain boundary energies. Appl. Math. Model. 2020;78:505–18.
[150] Holm EA, Hassold GN, Miodownik MA. On misorientation distribution evolution during anisotropic grain growth. Acta Mater 2001;49(15):2981–91.
[151] Miyoshi E, Takaki T. Multi-phase-field study of the effects of anisotropic grain-boundary properties on polycrystalline grain growth. J. Cryst. Growth 2017;474:160–5.
[152] Kazaryan A, Wang Y, Dregia S, Patton B. Grain growth in anisotropic systems: comparison of effects of energy and mobility. Acta Mater 2002;50(10):2491–502.
[153] Fausty J, Murgas B, Florez S, Bozzolo N, Bernacki M. A new analytical test case for anisotropic grain growth problems. Appl. Math. Model. 2021;93:28–52.
[154] Salama H, Kundin J, Shchyglo O, Mohles V, Marquardt K, Steinbach I. Role of inclination dependence of grain boundary energy on the microstructure evolution during grain growth. Acta Mater 2020;188:641–51.
[155] Viswanathan R, Bauer CL. Kinetics of grain boundary migration in copper bicrystals with [001] rotation axes. Acta Metall. 1973;21(8):1099–109.
[156] Demianczuk DW, Aust KT. Effect of solute and orientation on the mobility of near-coincidence tilt boundaries in high-purity aluminum. Acta Metall. 1975;23(10):1149–62.
[157] Maksimova EL, Shvindlerman LS, Straumal BB. Transformation of σ17 special tilt boundaries to general boundaries in tin. Acta Metall. 1988;36(6):1573–83.
[158] Gottstein G, Shvindlerman LS. On the true dependence of grain boundary migration rate on driving force. Scripta metallurgica et materialia 1992;27(11):1521–6.
[159] Winning M, Gottstein G, Shvindlerman LS. On the mechanisms of grain boundary migration. Acta Mater 2002;50(2):353–63.
[160] V.A. Ivanov, On kinetics and thermodynamics of high angle grain boundaries in aluminum: Experimental study on grain boundary properties in bi-and tricrystals, Tech. rep., Fakultät für Georessourcen und Materialtechnik (2006).
[161] Zhang J, Poulsen SO, Gibbs JW, Voorhees PW, Poulsen HF. Determining material parameters using phase-field simulations and experiments. Acta Mater 2017;129:229–38.
[162] Zhang J, Ludwig W, Zhang Y, Sørensen HHB, Rowenhorst DJ, Yamanaka A, Voorhees PW, Poulsen HF. Grain boundary mobilities in polycrystals. Acta Mater 2020;191:211–20.
[163] Juul Jensen D, Zhang Y. Impact of 3D/4D methods on the understanding of recrystallization. Curr. Opin. Solid State Mater. Sci. 2020;24(2):100821.
[164] Fang H, Juul Jensen D, Zhang Y. Improved grain mapping by laboratory X-ray diffraction contrast tomography. IUCrJ 2021;8(4):559–73.
[165] Janssens KG, Olmsted D, Holm EA, Foiles SM, Plimpton SJ, Derlet PM. Computing the mobility of grain boundaries. Nature materials 2006;5(2):124–7.
[166] Olmsted DL, Foiles SM, Holm EA. Survey of computed grain boundary properties in face-centered cubic metals: I. grain boundary energy. Acta Mater 2009;57(13):3694–703.
[167] Olmsted DL, Holm EA, Foiles SM. Survey of computed grain boundary properties in face-centered cubic metals—ii: Grain boundary mobility. Acta materialia 2009;57(13):3704–13.
[168] Fjeldberg E, Marthinsen K. A 3D Monte Carlo study of the effect of grain boundary anisotropy and particles on the size distribution of grains after recrystallisation and grain growth. Comput. Mater. Sci. 2010;48(2):267–81.
[169] Song Y-H, Wang M-T, Ni J, Jin J-F, Zong Y-P. Effect of grain boundary energy anisotropy on grain growth in zk60 alloy using a 3d phase-field modeling. Chin. Phys. B 2020;29(12):128201.
[170] Miyoshi E, Takaki T, Sakane S, Ohno M, Shibuta Y, Aoki T. Large-scale phase-field study of anisotropic grain growth: Effects of misorientation-dependent grain boundary energy and mobility. Comput. Mater. Sci. 2021;186:109992.
[171] Kim H-K, Ko W-S, Lee H-J, Kim SG, Lee B-J. An identification scheme of grain boundaries and construction of a grain boundary energy database. Scripta Mater. 2011;64(12):1152–5.
[172] Kim H-K, Kim SG, Dong W, Steinbach I, Lee B-J. Phase-field modeling for 3D grain growth based on a grain boundary energy database. Modell. Simul. Mater. Sci. Eng. 2014;22(3):034004.
[173] Read WT, Shockley W. Dislocation models of crystal grain boundaries. Phys. Rev. 1950;78(3):275–89.
[174] Hallberg H. Influence of anisotropic grain boundary properties on the evolution of grain boundary character distribution during grain growth—a 2d level set study. Modell. Simul. Mater. Sci. Eng. 2014;22(8):085005.
[175] Niño JD, Johnson OK. Influence of grain boundary energy anisotropy on the evolution of grain boundary network structure during 3d anisotropic grain growth. Comput. Mater. Sci. 2023;217:111879.
[176] GraGLeS2D software, https://github.com/GraGLeS/GraGLeS2D#gragles2d/.
[177] Murgas B, Florez S, Bozzolo N, Fausty J, Bernacki M. Comparative study and limits of different level-set formulations for the modeling of anisotropic grain growth. Materials 2021;14(14).
[178] M. Elsey, S. Esedoḡlu, Threshold dynamics for anisotropic surface energies, Mathematics of Computation 87 (312) (2018) 1721–1756.
[179] Olmsted DL, Foiles SM, Holm EA. Survey of computed grain boundary properties in face-centered cubic metals: I. grain boundary energy. Acta Mater 2009;57(13):3694–703. https://doi.org/10.1016/j.actamat.2009.04.007.
[180] Bulatov VV, Reed BW, Kumar M. Grain boundary energy function for fcc metals. Acta Mater 2014;65:161–75. https://doi.org/10.1016/j.actamat.2013.10.057.
[181] Bozzolo N, Bernacki M. Viewpoint on the formation and evolution of annealing twins during thermomechanical processing of fcc metals and alloys. Metallurgical and Materials Transactions A 2020;51(6):2665–84.
[182] Mackenzie J. Second paper on statistics associated with the random disorientation of cubes. Biometrika 1958;45(1–2):229–40.
[183] Huang K, Logé R. A review of dynamic recrystallization phenomena in metallic materials. Materials & Design 2016;111:548–74. https://doi.org/10.1016/j.matdes.2016.09.012.
[184] Grand V, Flipon B, Gaillac A, Bernacki M. Simulation of Continuous Dynamic Recrystallization Using a Level-Set Method. Materials 2022;15(23):8547. https://doi.org/10.3390/ma15238547.
[185] A. Gaillac, V. Grand, A. Arsen, Q. Gaillard, M. Bernacki, Towards multi-scale modeling of zirconium alloys recrystallization and application to thermo-mechanical processes optimization, in: Key Engineering Materials, Vol. 926, Trans Tech Publ, 2022, pp. 443–451.
[186] Gourdet S, Montheillet F. A model of continuous dynamic recrystallization. Acta Mater 2003;51(9):2685–99.
[187] Zener C. Theory of growth of spherical precipitates from solid solution. J. Appl. Phys. 1949;20(10):950–3.
[188] Manohar PA, Ferry M, Chandra T. Five Decades of the Zener Equation. ISIJ Int. 1998;38(1998):913–24.
[189] Srolovitz D, Anderson M, Grest G, Sahni P. Computer simulation of grain growth-iii. influence of a particle dispersion. Acta Metall. 1984;32(9):1429–38.
[190] Anderson M, Grest G, Doherty R, Li K, Srolovitz D. Inhibition of grain growth by second phase particles: Three dimensional monte carlo computer simulations. Scr. Metall. 1989;23(5):753–8.

[191] Hassold G, Holm E, Srolovitz D. Effects of particle size on inhibited grain growth. Scr. Metall. Mater. 1990;24(1):101–6.
[192] Gao J, Thompson RG, Patterson BR. Computer simulation of grain growth with second phase particle pinning. Acta Mater 1997;45(9):3653–8.
[193] Kad BK, Hazzledine PM. Monte carlo simulations of grain growth and zener pinning. Materials Science and Engineering: A 1997;238(1):70–7.
[194] Phaneesh KR, Bhat A, Mukherjee P, Kashyap KT. On the zener limit of grain growth through 2D Monte Carlo simulation. Comput. Mater. Sci. 2012;58:188–91.
[195] Weygand S, Brechet Y, Lépinoux J. Zener pinning and grain growth: A two-dimensional vertex computer simulation. Acta Mater 1999;47(3):961–70.
[196] Couturier G, Maurice C, Fortunier R. Three-dimensional finite-element simulation of Zener pinning dynamics. Phil. Mag. 2003;83(30):3387–405.
[197] Chang K, Feng W, Chen L. Effect of second-phase particle morphology on grain growth kinetics. Acta Mater 2009;57(17):5229–36.
[198] Tonks M, Zhang Y, Butterfield A, Bai X. Development of a grain boundary pinning model that considers particle size distribution using the phase field method. Modell. Simul. Mater. Sci. Eng. 2015;23(4):045009.
[199] Moelans N, Blanpain B, Wollants P. Phase field simulations of grain growth in two-dimensional systems containing finely dispersed second-phase particles. Acta Mater 2006;54(4):1175–84.
[200] Chang K, Moelans N. Effect of grain boundary energy anisotropy on highly textured grain structures studied by phase-field simulations. Acta Mater 2014;64:443–54.
[201] Agnoli A, Bernacki M, Logé R, Franchet J, Laigo J, Bozzolo N. Understanding and modeling of grain boundary pinning in Inconel 718. In: Superalloys 2012: The 12th international symposium on superalloys, Pennsylvania: United States; 2012.
[202] Scholtes B, Ilin D, Settefrati A, Bozzolo N, Agnoli A, Bernacki M. Full field modeling of the Zener pinning phenomenon in a level set framework - discussion of classical limiting mean grain size equation. In: Proceedings of the 13th International Symposium on Superalloys; 2016.
[203] Alvarado K, Florez S, Flipon B, Bozzolo N, Bernacki M. A level set approach to simulate grain growth with an evolving population of second phase particles. Modell Simul Mater Sci Eng 2021;29(3):035009.
[204] Alvarado K, Janeiro I, Florez S, Flipon B, Franchet J-M, Locq D, Dumont C, Bozzolo N, Bernacki M. Dissolution of the primary γ' precipitates and grain growth during solution treatment of three nickel base superalloys. Metals 2021;11(12).
[205] Settefrati A, De Micheli P, Maire L, Scholtes B, Bozzolo N, Moussa C, Perchat E, Bernacki M. Prediction of the grain size evolution during thermal treatments at the mesoscopic scale: a numerical framework and industrial examples. Matériaux & Techniques 2018;106(1):105. https://doi.org/10.1051/mattech/2018034.
[206] Digimu software, https://www.transvalor.com/en/digimu/.
[207] De Micheli P, Maire L, Cardinaux D, Moussa C, Bozzolo N, Bernacki M. DIGIMU: Full field recrystallization simulations for optimization of multi-pass processes. AIP Conf Proc 2019;2113(1):040014. https://doi.org/10.1063/1.5112548.
[208] De Micheli P, Alvarado K, Grand V, Bernacki M. Full field continuous dynamic recrystallization simulations considering precipitates evolutions with DIGIMU<error l="580" c="Undefined command "/>. In: Proceedings of the 27th International ESAFORM Conference on Material Forming; 2024.
[209] B. Scholtes, M. Shakoor, N. Bozzolo, P.-O. Bouchard, A. Settefrati, M. Bernacki, Advances in level-set modeling of recrystallization at the polycrystal scale - development of the digi-μ software, in: Material Forming ESAFORM 2015, Vol. 651 of Key Engineering Materials, Trans Tech Publications Ltd, 2015, pp. 617–623. doi:10.4028/www.scientific.net/KEM.651-653.617.
[210] James R. Displacive phase transformations in solids. J Mech Phys Solids 1986;34(4):359–94.
[211] Gamsjäger E, Antretter T, Schmaranzer C, Preis W, Chimani C, Simha N, Svoboda J, Fischer F. Diffusional phase transformation and deformation in steels. Comput Mater Sci 2002;25(1):92–9.
[212] Wheeler AA, Boettinger WJ, McFadden GB. Phase-field model for isothermal phase transitions in binary alloys. Phys Rev A 1992;45:7424–39.
[213] Tiaden J, Nestler B, Diepers H, Steinbach I. The multiphase-field model with an integrated concept for modelling solute diffusion. Physica D 1998;115(1):73–86.
[214] Chandrappa N, Bernacki M. A level-set numerical framework for the modeling of diffusive solid - solid phase transformation in the context of austenite decomposition. In: 15ème colloque national en calcul des structures, Université Polytechnique Hauts-de-France [UPHF], 83400 Hyères-les-Palmiers, France; 2022.
[215] Steinbach I, Böttger B, Eiken J, Warnken N, Fries S. Calphad and phase-field modeling: a successful liaison. J Phase Equilib Diffus 2007;28(1):101–6.
[216] Thermo-calc software, http://www.thermocalc.se/.
[217] Mecozzi M, Eiken J, Apel M, Sietsma J. Quantitative comparison of the phase-transformation kinetics in a sharp-interface and a phase-field model. Comput Mater Sci 2011;50(6):1846–53.
[218] Liu X, Li H, Zhan M. A review on the modeling and simulations of solid-state diffusional phase transformations in metals and alloys. Manuf Rev 2018;5:10.
[219] Mecozzi MG. Phase field modelling of the austenite to ferrite transformation in steels. Ph.D. thesis. Delf University of Technology; 2006.
[220] Steinbach I. Phase-field models in materials science. Modell Simul Mater Sci Eng 2009;17(7):073001. https://doi.org/10.1088/0965-0393/17/7/073001.
[221] Furstoss J, Petit C, Tommasi A, Ganino C, Muñoz DP, Bernacki M. On the role of solute drag in reconciling laboratory and natural constraints on olivine grain growth kinetics. Geophys J Int 2020;224(2):1360–70. https://doi.org/10.1093/gji/ggaa520.
[222] Hahn P, Gaillac A, Flipon B, Bignon M, Bozzolo N, Bernacki M. Characterization and modelling of grain growth in zr-nb alloys: niobium concentration influence. In: Proceedings of the 27th International ESAFORM Conference on Material Forming; 2024.
[223] Zouaghi A, Bellet M, Bienvenu Y, Perrin G, Cédat D, Bernacki M. Modelling of the compaction phase during Hot Isostatic Pressing process at the mesoscopic scale. Metal Powder Industries Federation 2012:3117.
[224] J. Bruchon, D. Pino-Muñoz, F. Valdivieso, S. Drapier, Finite Element Simulation of Mass Transport During Sintering of a Granular Packing. Part I. Surface and Lattice Diffusions, Journal of the American Ceramic Society 95 (8) (2012) 2398–2405. doi:10.1111/j.1551-2916.2012.05073.x.
[225] Bruchon J, Drapier S, Valdivieso F. 3D finite element simulation of the matter flow by surface diffusion using a level set method. Int J Numer Meth Eng 2011;86(7):845–61. https://doi.org/10.1002/nme.3079.
[226] D. Montes de Oca Zapiain, J.A. Stewart, R. Dingreville, Accelerating phase-field-based microstructure evolution predictions via surrogate models trained by machine learning methods, npj Computational Materials 7 (1) (2021) 3.
[227] Hashemi S, Kalidindi SR. A machine learning framework for the temporal evolution of microstructure during static recrystallization of polycrystalline materials simulated by cellular automaton. Comput Mater Sci 2021;188:110132.
[228] Oommen V, Shukla K, Goswami S, Dingreville R, Karniadakis GE. Learning two-phase microstructure evolution using neural operators and autoencoder architectures. npj Comput Mater 2022;8(1):190.
[229] Yan W, Melville J, Yadav V, Everett K, Yang L, Kesler MS, Krause AR, Tonks MR, Harley JB. A novel physics-regularized interpretable machine learning model for grain growth. Mater Des 2022;222:111032.